

# Water Mass Transformation Budgets in Finite-Volume Generalized Vertical Coordinate Ocean Models

Henri. F. Drake<sup>1</sup>, Shanice Bailey<sup>2</sup>, Raphael Dussin<sup>3,5</sup>, Stephen M. Griffies<sup>4,5</sup>,  
John Krasting<sup>5</sup>, Graeme MacGilchrist<sup>6</sup>, Geoffrey Stanley<sup>7</sup>, Jan-Erik Tesdal<sup>4</sup>,  
Jan D. Zika<sup>8,9</sup>

<sup>1</sup>Department of Earth System Science, University of California Irvine, Irvine, CA, USA

<sup>2</sup>Columbia University, Department of Earth and Environmental Sciences, NY, USA

<sup>3</sup>University Corporation for Atmospheric Research, Boulder, CO, USA

<sup>4</sup>Princeton University Program in Atmospheric and Oceanic Sciences, Princeton, NJ, USA

<sup>5</sup>NOAA Geophysical Fluid Dynamics Laboratory, Princeton, NJ, USA

<sup>6</sup>School of Earth and Environmental Sciences, University of St. Andrews, Scotland

<sup>7</sup>School of Earth and Ocean Sciences, University of Victoria, Canada

<sup>8</sup>School of Mathematics and Statistics, University of New South Wales, Australia

<sup>9</sup>Australian Centre for Excellence in Antarctic Science, University of New South Wales, Australia

## Key Points:

- Water mass budgets provide insights into the processes transforming material water mass properties and how they relate to circulation.
- Spurious water mass transformations due to advection scheme errors can be quantified by combining mass and tracer budget diagnostics.
- We describe best practices for model analysis and present a novel Python stack for model-agnostic and out-of-memory regional calculations.

---

Corresponding author: Henri Drake, [hfdrake@uci.edu](mailto:hfdrake@uci.edu)

**Abstract**

Water mass transformation theory provides conceptual tools that in principle enable innovative analyses of numerical ocean models; in practice, however, these methods can be challenging to implement and interpret, and therefore remain under-utilized. Our aim is to demonstrate the feasibility of diagnosing all terms in the water mass budget and to exemplify their usefulness for scientific inquiry and model development by quantitatively relating water mass changes, overturning circulations, boundary fluxes, and interior mixing.

We begin with a pedagogical derivation of key results of classical water mass transformation theory. We then describe best practices for diagnosing each of the water mass budget terms from the output of Finite-Volume Generalized Vertical Coordinate (FV-GVC) ocean models, including the identification of a non-negligible remainder term as the spurious numerical mixing due to advection scheme discretization errors. We illustrate key aspects of the methodology through an example application to diagnostics from a polygonal region of a Baltic Sea regional configuration of the Modular Ocean Model v6 (MOM6). We verify the convergence of our WMT diagnostics by brute-force, comparing time-averaged diagnostics on various vertical grids to timestep-averaged diagnostics on the native model grid. Finally, we briefly describe a stack of xarray-enabled Python packages for evaluating WMT budgets in FV-GVC models, which is intended to be model-agnostic and available for community use and development.

**Plain Language Summary**

A useful tool for characterizing ocean variability and change is water mass analysis, in which the ocean is decomposed into parcels with distinct properties (such as their temperature, density, or dissolved oxygen concentrations). Water mass transformation theory provides a concise equation for the evolution of these water masses, which can be used to identify the various processes that act to increase or decrease the total mass (or size) of each parcel. In practice, however, calculating the terms in these WMT budget equations from ocean model simulation output is technically challenging, limiting the creativity of applications in the literature. We review the fundamentals of water mass transformation theory, explain how to calculate WMT budgets based on the output of a generic ocean model simulation (with examples from a widely used one), and summarize a new publicly-available software for doing such calculations.

**1 Introduction**

The mean state, intrinsic variability, and forced changes of the global ocean can be usefully characterized by dividing waters into several distinct *water masses* and analyzing their respective steady balances or transient evolutions (Sverdrup et al., 1942). Each such water mass is defined by the intersection of bounds on scalar tracer concentrations and/or fixed spatial coordinates that define a region of the globe. (For convenience, we use the term ‘water mass’ to refer to both the region that it occupies in space,  $\Omega$ , as well as the total mass of seawater in the region,  $\mathcal{M}_\Omega$ ; it will be clear which is meant from context and notation.) The ocean’s global overturning circulation, for example, is canonically described as the circulation of water masses through latitude-density space (Döös & Webb, 1994; Lumpkin & Speer, 2007; Cessi, 2019). Since density variations exert a significant control on oceanic flow, it is common to categorizing water masses in distinct density classes. Seawater density itself depends nonlinearly on temperature and salinity (and pressure), which due to their different boundary conditions are partially independent and are thus used to further distinguish water masses. Passive tracers, especially dissolved or particulate biogeochemical substances, also serve as effective water mass tags (Broecker, 1982). We focus here on water masses defined by bounds on a single scalar (e.g., temperature, density, or tracer concentration) but acknowledge that

72 it can be beneficial to consider the intersections of bounds on multiple tracers (e.g., to  
73 analyze the thermohaline streamfunction as in Zika et al. (2012); Döös et al. (2012); Groeskamp  
74 et al. (2014)). Throughout the text, we denote surfaces of constant scalar values as *isoscalar*  
75 surfaces and the direction normal to isoscalar surfaces (in the direction of increasing scalar  
76 value) as *diascalar*.

77 In water mass analysis, ocean variability and change is understood as the variabil-  
78 ity and change of its constituent water *masses*. Kinematically, water mass change refers  
79 to the movement of the isoscalar surfaces that bound the water mass. For instance, the  
80 observed contraction of Antarctic Bottom Waters corresponds to the deepening of their  
81 bounding isopycnal surface due to decades of abyssal warming and freshening (Purkey  
82 & Johnson, 2012). The utility of a particular tracer for water mass analysis depends on  
83 how its source/sink and transport processes relate to the problem at hand. Water mass  
84 analysis has long been used by oceanographers to infer patterns of large-scale ocean cir-  
85 culation from tracers with long residence times and known sources/sinks. Early anal-  
86 yses (e.g., Iselin (1939)) were carried out qualitatively and by hand, while more recent  
87 analyses employ numerical models on fixed Eulerian grids.

88 A major conceptual breakthrough was Walin (1982)’s introduction of Water Mass  
89 Transformation (WMT) theory, which directly equates the kinematic evolution and cir-  
90 culation of water masses to the various transformation processes that drive material change.  
91 Tziperman (1986), A. J. G. Nurser et al. (1999), Marshall et al. (1999), Iudicone et al.  
92 (2008) and others further developed important aspects of the theory. Groeskamp et al.  
93 (2019) present a modern treatment of WMT fundamentals and review various applica-  
94 tions in the literature; our purpose here is not to repeat this exercise but instead to com-  
95 plement it by detailing how each of the terms in a water mass budget should be diag-  
96 nosed and interpreted in the context of finite-volume ocean models. Calculations of full  
97 water mass transformation budgets are rare in the literature, reflecting the scarcity of  
98 necessary diagnostics and the technical difficulty of implementing methods consistent with  
99 increasingly complicated numerical model formulations. The difficulty of closing WMT  
100 budgets motivates a common use case, which is to assume a closed budget and simply  
101 bundle any neglected terms into a remainder (e.g. Tesdal et al., 2023; Evans et al., 2023).  
102 Many go even further, assuming the water mass distribution to be in steady state and  
103 thus identifying the remainder of the water mass transformation terms as the diascalar  
104 overturning transport (de Lavergne et al., 2016; Ferrari et al., 2016). A major caveat of  
105 all these indirect inference approaches is that any errors in the explicitly calculated terms—  
106 whether observational, computational, or conceptual in nature—are obscured by bundling  
107 them into the remainder along with the neglected terms; this total remainder term is of-  
108 ten found to be of leading order, calling into question interpretations of WMT budget  
109 results. A more careful analysis would evaluate every term in the budget and confirm  
110 that the remainder is zero—or at least sufficiently small to not affect the interpretation  
111 of results (see Lele et al. (2021) for an observation-based example of an approximately  
112 closed full WMT budget).

113 A related but more subtle problem with model-based water mass analysis regards  
114 spurious water mass transformation due to numerical mixing, which is the effective di-  
115 ascalar mixing induced by artificial diffusive and dispersive errors in a discretized tracer  
116 advection scheme (Molenkamp, 1968). Spurious water mass transformations in density  
117 space (i.e. diapycnal) are particularly concerning because diapycnal mixing plays a leading-  
118 order role in ocean dynamics and energetics (Toggweiler & Samuels, 1998; Ferrari & Wun-  
119 sch, 2009) and because measured diapycnal mixing rates are small enough that they can  
120 be easily overwhelmed by numerical errors (Griffies et al., 2000; Lee et al., 2002). Current-  
121 generation ocean and climate models still suffer from significant biases which can be traced  
122 to excessive diapycnal mixing, much of which is thought to be due to spurious numer-  
123 ical mixing as opposed to over-tuned mixing parameterizations (Fox-Kemper et al., 2019).  
124 Reducing spurious diapycnal mixing thus remains a priority of ocean model development

125 and a driver of major model configuration choices, such as the adoption of isopycnal or  
 126 hybrid generalized vertical coordinates (e.g., Adcroft et al., 2019; Griffies et al., 2020).  
 127 Despite the importance of numerical mixing for both the development of ocean models  
 128 and their application for scientific research, there is no consensus on the best practices  
 129 for quantifying it, and no open-source community diagnostics are presently available. Let  
 130 us briefly review some of the key approaches for quantifying numerical mixing in the lit-  
 131 erature and describe each of their limitations, motivating our novel approach here.

132 In their formative analysis, Griffies et al. (2000) apply Winters et al. (1995)’s avail-  
 133 able potential energy-based framework to diagnose spurious diapycnal mixing from er-  
 134 roneous increases in background potential energy in explicitly ‘adiabatic’ idealized flows.  
 135 This background potential energy approach is invasive in that it requires temporarily ‘spin-  
 136 ning down’ a diabatic model in a counterfactual adiabatic configuration; a limitation of  
 137 this approach is that the spurious mixing inferred from the adiabatic configuration does  
 138 not necessarily correspond to that of the diabatic configuration of interest. Ilıcak et al.  
 139 (2012) apply this method to a suite of idealized and realistic ocean model configurations,  
 140 and demonstrate that numerical mixing is highest in an eddying depth-coordinate model.  
 141 The interpretation of such results requires additional humility, however, because the cal-  
 142 culation of background potential energy by globally sorting the density field is ill-posed  
 143 for global ocean models with nonlinear equations of state and topography that dynam-  
 144 ically decouples ocean basins (Huang, 2005; Stewart et al., 2014; Saenz et al., 2015). Hill  
 145 et al. (2012) propose an approach based on the diapycnal spreading of passive tracers;  
 146 however, this approach is not scalable to global climate models configurations due to the  
 147 many additional passive tracers that would need to be integrated. Drake et al. (2022)  
 148 raise a more fundamental problem with the tracer-based approach: a tracer’s diapycnal  
 149 spreading rate is not exactly proportional to tracer-weighted diffusivity. Burchard and  
 150 Rennau (2008) propose a tracer variance approach motivated by turbulence studies, which  
 151 offers the means to map where spurious mixing occurs. However, it provides a three-dimensional  
 152 effective diffusivity and so does not distinguish between diapycnal and isopycnal. Given  
 153 these caveats and limitations of the above methods, we would like a more robust met-  
 154 ric of spurious diascalar mixing that can be: 1) directly compared to parameterized dis-  
 155 calscalar mixing processes, 2) efficiently and unintrusively diagnosed, and 3) unambigu-  
 156 ously interpreted.

157 Lee et al. (2002) pioneered a promising approach for diagnosing spurious diapyc-  
 158 nal mixing as the remainder of a model’s WMT budget, which in principle allows spu-  
 159 rious mixing to be directly compared against other terms in the mass budget. Lee et al.  
 160 (2002)’s analysis suggests that spurious diapycnal mixing is an order of magnitude larger  
 161 than the parameterized vertical mixing in their model, although they invoke some ques-  
 162 tionable assumptions to close the mass budget without directly diagnosing transforma-  
 163 tions due to parameterized diffusion or surface fluxes. Megann (2018) improve upon this  
 164 approach by directly comparing effective diapycnal transports with those implied by pa-  
 165 rameterized mixing, attributing the difference between the two to spurious numerical mix-  
 166 ing. Urakawa and Hasumi (2012) and Urakawa and Hasumi (2014) extend the approach  
 167 by evaluating every term in the WMT budget and identifying the remainder as the spu-  
 168 rious water mass transformation, without resorting to approximations or expressing the  
 169 results in terms of an ‘effective’ numerical diffusivity. (They additionally propose a method  
 170 for decomposing spurious numerical mixing into cabbeling and non-cabbeling compo-  
 171 nents, but this requires implementing intrusive new diagnostics, so we neglect it here for  
 172 simplicity). Bailey et al. (2023) generalizes the approach from latitudinal coordinates to  
 173 a rectangular region with vertical walls. An important caveat of the above WMT bud-  
 174 get calculations is that they consider transformations across potential density surfaces  
 175 (often referenced to either surface pressures  $p = p_{\text{atm}} \approx 0$  dbar, denoted  $\rho_0$ , or a mid-  
 176 depth pressure of 2000 dbar, denoted  $\rho_2$ ). Because potential density surfaces deviate sig-  
 177 nificantly from neutrality away from their reference pressure, purely isoneutral processes  
 178 can misleadingly appear to induce diapycnal transformations, potentially leading to mis-

179 interpretation of results (see T. J. McDougall et al. (2014) as well as the discussion in  
 180 Section 4). Iudicone et al. (2008) address these limitations by diagnosing water mass trans-  
 181 formations across approximately neutral density  $\gamma^n$  surfaces (as defined by Jackett and  
 182 McDougall (1997)); however, they do not diagnose all of the terms in the WMT bud-  
 183 get and thus do not isolate the contributions from spurious numerical mixing. A prac-  
 184 tical limitation of each of these approaches is that the calculation of lateral transport  
 185 terms is tailored to the particular analysis, such that it would take a considerable effort  
 186 to replicate the analysis for 1) a different region, 2) a model with a different grid or bud-  
 187 get diagnostics, or 3) with respect to a different tracer. Holmes et al. (2021) cleverly sidestep  
 188 the two challenging aspects of WMT analysis described above—nonlinear equation of state  
 189 effects and the diagnosis of lateral transports across complicated regional boundaries—  
 190 by framing their analysis in terms of *diathermal* fluxes and by diagnosing budget terms  
 191 in *individual grid columns*.

192 We present a theoretically precise and numerically accurate approach for diagnos-  
 193 ing closed WMT budgets in Finite-Volume ocean models with Generalized Vertical Co-  
 194 ordinates (FV-GVC models). The following self-contained derivations of the theory are  
 195 inspired by the water mass transformation framework introduced by Walin (1982), re-  
 196 cently reviewed by Groeskamp et al. (2019), and extended to the numerical modeling con-  
 197 text by Lee et al. (2002), Urakawa and Hasumi (2012), and Bailey et al. (2023). Because  
 198 the derivations in these prior texts leave out many details and pass over some important  
 199 theoretical and practical aspects of water mass analysis, we present a more complete and  
 200 pedagogical derivation of the fundamental equations of water mass analysis. We argue  
 201 that this level of care is necessary to 1) correctly close regional WMT budgets, 2) con-  
 202 fidently attribute the remainder term to spurious numerical mixing, and 3) robustly in-  
 203 terpret the balance of terms in the budget.

204 Section 2 presents the continuous theory and Section 3 describes how each of these  
 205 terms is diagnosed in practice, including the identification of the remainder term with  
 206 spurious numerical mixing (Section 3.5). Section 4 concludes with a future outlook dis-  
 207 cussion, including discussions of unconventional WMT analyses and important subtleties  
 208 of WMT calculations in density space. Appendix A describes the relationship between  
 209 the continuous theory (Section 2) and the layer-integrated mass and tracer budget di-  
 210 agnostics provided by FV-GVC models (used for the calculations in Section 3). Appendix  
 211 B describes how these terms correspond to diagnostics available in the Modular Ocean  
 212 Model v6 (MOM6; Adcroft et al. (2019)). In Appendix C we discuss some theoretical  
 213 aspects of WMT budgets under the Boussinesq approximation, which is employed by many  
 214 commonly used FV-GVC ocean models and often assumed in WMT analyses. Appendix  
 215 D describes the core open-source Python package (`xwmb`) developed to carry out these  
 216 WMT budget calculations, as well as the stack of packages it depends on, which are all  
 217 intended to be model-agnostic and available for use by the ocean modeling community.  
 218 Throughout, we provide illustrations of theoretical concepts and examples of numerical  
 219 calculations based on diagnostics from a year-long ocean-only simulation in a regional  
 220 Baltic Sea configuration of MOM6 at a nominal horizontal grid spacing of  $0.25^\circ$ . Ongo-  
 221 ing extensions of the work to global OM4 (Adcroft et al., 2019) and CM4 (Held et al.,  
 222 2019) outputs and approximately neutral density coordinates (following Stanley et al.  
 223 (2021)) are beyond the scope of this paper and will be described elsewhere.

## 224 **2 Theory: kinematics of $\lambda$ -water masses and their transformations**

### 225 **2.1 Evolution of $\lambda$ -water masses**

226 We are interested in the evolution of bulk water masses defined by contours  $\{\tilde{\lambda}\}$   
 227 of a single given scalar  $\lambda(\mathbf{x}, t)$ , which we here define as the class of waters with  $\lambda(\mathbf{x}, t) \leq$

228  $\tilde{\lambda}$ . The key metric that characterizes a water mass is, unsurprisingly, its mass

$$\mathcal{M}(\tilde{\lambda}, t) \equiv \int_{\lambda(\mathbf{x}, t) \leq \tilde{\lambda}} \rho dV, \quad (1)$$

229 where  $\rho(\mathbf{x}, t)$  is the seawater density *in situ* and  $dV$  is the volume element. More gen-  
 230 erally, we can consider the intersection  $\Omega(\tilde{\lambda}, t) \equiv \{\mathbf{x} : \lambda(\mathbf{x}, t) < \tilde{\lambda}\} \cap \mathcal{R}$  of this global  
 231 water mass definition with an arbitrary time-varying spatial region of the ocean,  $\mathcal{R}(t)$ .  
 232 We emphasize that the water mass region  $\Omega$  need not be contiguous. The water mass  
 233 region  $\Omega$  is characterized by the sub-mass

$$\mathcal{M}_{\Omega}(\tilde{\lambda}, t) \equiv \int_{\Omega(\tilde{\lambda}, t)} \rho dV \leq \mathcal{M}(\tilde{\lambda}, t). \quad (2)$$

234 For example, if  $\mathcal{R}$  is the Southern Ocean south of 30°S, then we identify  $\Omega(1^{\circ}\text{C}, t) =$   
 235  $\{\mathbf{x} : \Theta(\mathbf{x}, t) < 1^{\circ}\text{C}\} \cap \mathcal{R}$  as the mass of cold waters around Antarctica.

236 The complementary water mass that is instead bounded from below,  $\mathcal{M}_{\Omega}^{\dagger}(\tilde{\lambda}, t) \equiv$   
 237  $\int_{\tilde{\lambda} < \lambda} \rho dV$ , is simply derived as  $\mathcal{M}_{\Omega}^{\dagger}(\tilde{\lambda}, t) = \mathcal{M}_{\mathcal{R}} - \mathcal{M}_{\Omega}(\tilde{\lambda}, t)$ , where  $\mathcal{M}_{\mathcal{R}} \equiv \mathcal{M}_{\Omega}(\tilde{\lambda} \rightarrow$   
 238  $+\infty)$  is the total seawater mass in the region  $\mathcal{R}$ . Similarly, intermediate water masses  
 239 are defined by  $\mathcal{M}_{\Omega}(\tilde{\lambda}_1; \tilde{\lambda}_2) \equiv \int_{\tilde{\lambda}_1 < \lambda' \leq \tilde{\lambda}_2} \rho dV = \mathcal{M}_{\Omega}(\tilde{\lambda}_2) - \mathcal{M}_{\Omega}(\tilde{\lambda}_1)$ .

240 To understand the evolution of  $\mathcal{M}_{\Omega}(\tilde{\lambda}, t)$  over time, we start by integrating the sea-  
 241 water mass conservation equation,

$$\frac{\partial \rho}{\partial t} = -\nabla \cdot (\rho \mathbf{v}), \quad (3)$$

242 over the spatial extent of the water mass  $\Omega(\tilde{\lambda}, t)$ . Invoking the divergence theorem, we  
 243 have

$$\int_{\Omega(\tilde{\lambda}, t)} \frac{\partial \rho}{\partial t} dV = - \int_{\Omega(\tilde{\lambda}, t)} \nabla \cdot (\rho \mathbf{v}) dV = - \oint_{\partial\Omega(\tilde{\lambda}, t)} \rho \mathbf{v} \cdot \hat{\mathbf{n}} dS, \quad (4)$$

244 where we define  $\partial\Omega$  as the surface that bounds  $\Omega$  and  $\hat{\mathbf{n}}$  is the outward normal unit vec-  
 245 tor. Since the water mass  $\Omega(\tilde{\lambda}, t)$  is time-varying, time derivatives do not commute with  
 246 the density-weighted volume integral:

$$\frac{\partial}{\partial t} \mathcal{M}_{\Omega}(\tilde{\lambda}, t) \equiv \frac{\partial}{\partial t} \int_{\Omega(\tilde{\lambda}, t)} \rho dV \neq \int_{\Omega(\tilde{\lambda}, t)} \frac{\partial \rho}{\partial t} dV. \quad (5)$$

247 Hence, we cannot simply pull the time derivative on the left-hand side (LHS) of equa-  
 248 tion (4) out of the volume integral. Instead, we must invoke the three-dimensional gen-  
 249 eralization of Leibniz' integral rule (also known as Leibniz-Reynolds' transport theorem),  
 250 which accounts for the time-evolving bounds of integration through an additional term:

$$\frac{\partial}{\partial t} \int_{\Omega(\tilde{\lambda}, t)} F dV = \int_{\Omega(\tilde{\lambda}, t)} \frac{\partial F}{\partial t} dV + \oint_{\partial\Omega(\tilde{\lambda}, t)} F \mathbf{v}^{(\partial\Omega)} \cdot \hat{\mathbf{n}} dS, \quad (6)$$

251 where  $F(\mathbf{x}, t)$  is an arbitrary scalar function and  $\mathbf{v}^{(\partial\Omega)}$  is the velocity of the boundary  
 252  $\partial\Omega$  itself. A nonzero boundary velocity  $\mathbf{v}^{(\partial\Omega)}$  can occur as a result of movement in ei-  
 253 ther the bounding  $\tilde{\lambda}$ -isosurface or the boundaries of the region  $\mathcal{R}$ . The boundary veloc-  
 254 ity is generally decoupled from the fluid velocity; the important exception is for a mater-  
 255 ial region that follows the flow, in which

$$\mathbf{v}^{(\partial\Omega)} \cdot \hat{\mathbf{n}} = \mathbf{v} \cdot \hat{\mathbf{n}} \quad (\text{material region}). \quad (7)$$

256 Applying equation (6) to the case of  $F = \rho$  and combining with equation (4), we find  
 257 that  $\lambda$ -water mass evolution is determined by a balance between flow convergence within  
 258 the water mass and the movement of the water mass' boundary:

$$\frac{\partial}{\partial t} \mathcal{M}_{\Omega}(\tilde{\lambda}, t) \equiv \frac{\partial}{\partial t} \int_{\Omega(\tilde{\lambda}, t)} \rho dV = - \oint_{\partial\Omega(\tilde{\lambda}, t)} \rho (\mathbf{v} - \mathbf{v}^{(\partial\Omega)}) \cdot \hat{\mathbf{n}} dS. \quad (8)$$

259 This form of equation (8) is useful because the surface integral can be evaluated sepa-  
 260 rately for each of the different categories of the water mass boundary,  $\partial\Omega$ .

## 261 2.2 Characterizing dia-surface transport and boundary conditions

262 For an arbitrary region  $\mathcal{R}$  of the ocean (e.g., Figure 1), we consider four distinct  
 263 categories of water mass boundaries: the sea floor, the sea surface, interior  $\lambda$ -isosurfaces,  
 264 and any remaining boundaries of  $\mathcal{R}$  that do not fall under one of the other categories.  
 265 We can thus evaluate the total surface integral by considering the disjoint union

$$\partial\Omega(\tilde{\lambda}, t) \equiv \partial\Omega_{\text{seafloor}}(\tilde{\lambda}, t) \sqcup \partial\Omega_{\text{surf}}(\tilde{\lambda}, t) \sqcup \mathcal{A}_{\mathcal{R}}(\tilde{\lambda}, t) \sqcup \partial\mathcal{R}. \quad (9)$$

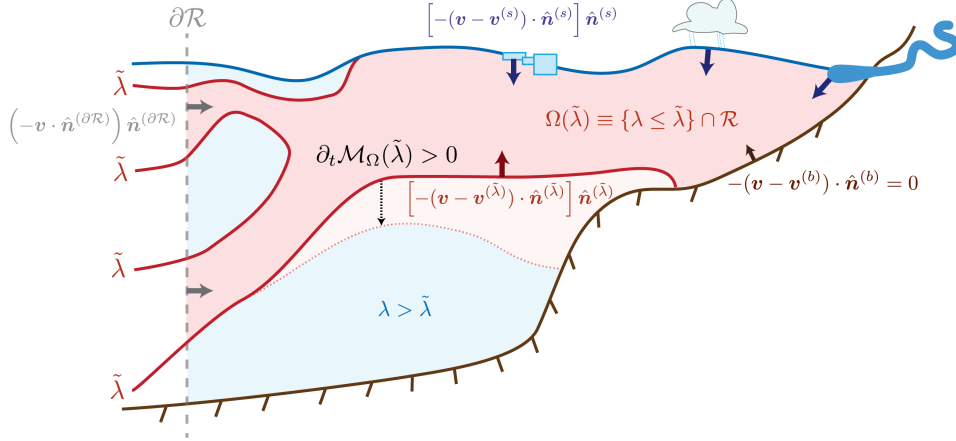


**Figure 1.** A schematic  $(x, z)$  profile view of the  $\lambda$ -water mass budget (equation (8)) for a water mass  $\Omega(\tilde{\lambda}, t)$  defined by the region  $\mathcal{R}$  and tracer values that satisfy  $\lambda(\mathbf{x}, t) \leq \tilde{\lambda}$  for a specific choice of  $\tilde{\lambda}$ . Note that  $\lambda$  is not required to be monotonic with depth and it is possible for multiple isosurfaces of  $\lambda$  to exist within a single vertical profile. The water mass  $\Omega(\tilde{\lambda}, t)$  is bounded by the seafloor (brown), sea surface (blue), interior  $\lambda$ -isosurfaces (red), and a specified regional boundary  $\partial\mathcal{R}$  (grey dashed). Water mass changes are due to mass fluxes across each of these boundaries, except the impermeable seafloor.

266

267 **Boundary 1: the seafloor.** The seafloor is assumed to be static ( $\mathbf{v}^{(b)} = 0$ ), trivially  
 268 leading to  $\rho \mathbf{v}^{(b)} \cdot \hat{\mathbf{n}}^{(b)} = 0$ . It is also impermeable to fluid flow, so that  $\rho \mathbf{v} \cdot \hat{\mathbf{n}}^{(b)} = 0$ .

269 **Boundary 2: the sea surface.** The sea surface, on the other hand, is time dependent  
 270 and permeable, allowing for exchanges of mass due to processes like precipitation, evap-  
 271 oration, sea ice freezing/melting, river inflow, etc. Following section 4 of A. G. Nurser  
 272 and Griffies (2019), this transport condition is given by

$$\rho (\mathbf{v} - \mathbf{v}^{(s)}) \cdot \hat{\mathbf{n}}^{(s)} = -Q_{\text{M}}^{\text{surf}}, \quad (10)$$

273 where  $\mathcal{Q}_M^{\text{surf}}$  is the net mass flux crossing the boundary per unit surface area due to the  
 274 various exchange processes mentioned above. We thus define the net surface mass flux  
 275 into the water mass as

$$\mathcal{S}_\Omega(\tilde{\lambda}, t) \equiv - \int_{\partial\Omega_{\text{surf}}(\tilde{\lambda}, t)} \rho(\mathbf{v} - \mathbf{v}^{(s)}) \cdot \hat{\mathbf{n}}^{(s)} dS = \int_{\partial\Omega_{\text{surf}}(\tilde{\lambda}, t)} \mathcal{Q}_M^{\text{surf}} dS. \quad (11)$$

276 In practice, it is more convenient to work in terms of the horizontal projection of  $dS$ , which  
 277 we write as  $dA$ , and thus define the normalized surface mass flux

$$Q_M^{\text{surf}} \equiv \mathcal{Q}_M^{\text{surf}} dS/dA, \quad (12)$$

278 which we use hereafter.

279 **Boundary 3: interior  $\tilde{\lambda}$ -isosurfaces.** This surface is the boundary between the re-  
 280 gions in  $\mathcal{R}$  where  $\lambda < \tilde{\lambda}$  and  $\lambda > \tilde{\lambda}$ , with normal vector  $\hat{\mathbf{n}}^{(\tilde{\lambda})} = \nabla\lambda/|\nabla\lambda|$ . Note that,  
 281 so long as  $\lambda$  is continuous,  $|\nabla\lambda| > 0$  on the  $\tilde{\lambda}$ -isosurface. We defer the further treatment  
 282 of this case to Section 2.3, where we relate the density-weighted dia- $\tilde{\lambda}$  velocity,  $(\mathbf{v} - \mathbf{v}^{(\tilde{\lambda})}) \cdot$   
 283  $\hat{\mathbf{n}}^{(\tilde{\lambda})}$ , to the kinematic material time derivative that appears in the  $\lambda$  conservation equa-  
 284 tion (16). The density-weighted dia- $\tilde{\lambda}$  velocity is then integrated along the  $\lambda = \tilde{\lambda}$  iso-  
 285 surface,  $\mathcal{A}_\mathcal{R}(\tilde{\lambda}, t)$ , which we again emphasize need not be contiguous or single-valued in  
 286 a water column.

287 **Boundary 4: specified regional boundaries.** Finally, the velocities of (and across)  
 288 the remaining surfaces of  $\partial\Omega(\tilde{\lambda}, t)$  depend on the definition of the specified region of in-  
 289 terest,  $\mathcal{R}(t)$ . When  $\mathcal{R}$  is the global ocean, for example, the other three boundaries al-  
 290 ready constitute all of  $\partial\Omega$  and this term vanishes. Another useful limit is when  $\mathcal{R}$  is time-  
 291 independent, such that  $\mathbf{v}^{(\partial\mathcal{R})} = 0$ , and we only need consider the contribution from the  
 292 cross-boundary flow,  $\mathbf{v} \cdot \hat{\mathbf{n}}^{(\partial\mathcal{R})}$ . A further simplifying assumption, which has been adopted  
 293 in most prior regional water mass transformation analyses (including Groeskamp et al.  
 294 (2019) and Bailey et al. (2023)) and will be employed hereafter, is that the region has  
 295 vertical boundaries. In this case,  $\hat{\mathbf{z}} \cdot \hat{\mathbf{n}}^{(\partial\mathcal{R})} = 0$  such that  $\mathbf{v} \cdot \hat{\mathbf{n}}^{(\partial\mathcal{R})}$  depends only on the  
 296 horizontal velocity

$$\mathbf{u} \equiv (\mathbf{v} \cdot \hat{\mathbf{x}}) \hat{\mathbf{x}} + (\mathbf{v} \cdot \hat{\mathbf{y}}) \hat{\mathbf{y}}. \quad (13)$$

297 We define the net convergent horizontal mass transport across the region's boundaries  
 298  $\partial\mathcal{R}$  (see Figure 1) as

$$\Psi_{\partial\mathcal{R}}(\tilde{\lambda}, t) \equiv - \int_{\partial\mathcal{R} \cap \{\lambda \leq \tilde{\lambda}\}} \rho \mathbf{u} \cdot \hat{\mathbf{n}}^{(\partial\mathcal{R})} dS, \quad (14)$$

299 where the surface integral includes the vertical boundaries of the region, where  $\lambda \leq \tilde{\lambda}$ .

300 **Altogether**, the  $\lambda$ -water mass budget equation (8) within the region  $\mathcal{R}$  can thus be writ-  
 301 ten as

$$\frac{\partial}{\partial t} \mathcal{M}_\Omega(\tilde{\lambda}, t) = \mathcal{S}_\Omega(\tilde{\lambda}, t) - \int_{\mathcal{A}_\mathcal{R}(\tilde{\lambda}, t)} \rho(\mathbf{v} - \mathbf{v}^{(\tilde{\lambda})}) \cdot \hat{\mathbf{n}}^{(\tilde{\lambda})} dS + \Psi_{\partial\mathcal{R}}(\tilde{\lambda}, t). \quad (15)$$

302 While equation (15) is conceptually straightforward, the surface integral appearing on  
 303 the right-hand side (RHS) is unwieldy and challenging to diagnose from both observa-  
 304 tion and models; we derive a more tractable expression for it in the following section.

### 305 2.3 Dia- $\tilde{\lambda}$ transport and water mass transformation

306 The natural starting point for developing a better understanding of the drivers of  
 307 dia- $\tilde{\lambda}$  transport is the conservation equation for the tracer concentration  $\lambda$ ,

$$\frac{D\lambda}{Dt} \equiv \frac{\partial\lambda}{\partial t} + \mathbf{v} \cdot \nabla\lambda = \dot{\lambda}, \quad (16)$$

308 where  $\frac{D}{Dt}$  is the material time derivative (which is the total time derivative computed  
 309 following the fluid flow) and  $\dot{\lambda}$  represents the sum of all processes that modify or trans-  
 310 form the  $\lambda$  concentration along that trajectory. Example processes leading to transfor-  
 311 mation include boundary exchange fluxes, molecular (or parameterized turbulent) dif-  
 312 fusion, and internal tracer sources or sinks (e.g. chemical reactions, ecological species in-  
 313 teractions, or radioactive decay). Multiplying equation (16) by  $\rho/|\nabla\lambda|$  and integrating  
 314 along the  $\lambda = \tilde{\lambda}$  isosurface within  $\mathcal{R}$ , denoted  $\mathcal{A}_{\mathcal{R}}(\tilde{\lambda}, t)$ , we arrive at

$$\int_{\mathcal{A}_{\mathcal{R}}(\tilde{\lambda}, t)} \frac{\rho}{|\nabla\lambda|} \frac{\partial\lambda}{\partial t} dS + \int_{\mathcal{A}_{\mathcal{R}}(\tilde{\lambda}, t)} \rho \mathbf{v} \cdot \frac{\nabla\lambda}{|\nabla\lambda|} dS = \int_{\mathcal{A}_{\mathcal{R}}(\tilde{\lambda}, t)} \frac{\rho \dot{\lambda}}{|\nabla\lambda|} dS. \quad (17)$$

315 Dividing by  $|\nabla\lambda|$  requires that it not vanish anywhere along the  $\tilde{\lambda}$ -isosurface  $\mathcal{A}_{\mathcal{R}}(\tilde{\lambda}, t)$ ;  
 316 while this may at first seem like a stringent constraint, however, it will always be the case  
 317 so long as  $\lambda$  is continuous. Note that it is perfectly fine for one or two components of the  
 318 gradient to vanish, as in the case of vertical overturns, but the three-dimensional gra-  
 319 dient will not vanish on any point on the surface as this would imply the point ceases  
 320 to be on the boundary between where  $\lambda < \tilde{\lambda}$  and  $\lambda > \tilde{\lambda}$ , which is the definition of the  
 321 isosurface. In the second term on the LHS of the isosurface-integrated equation (17), we  
 322 recognize  $\hat{\mathbf{n}}^{(\tilde{\lambda})} \equiv \nabla\lambda/|\nabla\lambda|$  as the unit vector normal to the  $\tilde{\lambda}$ -isosurface, thus identi-  
 323 fying this term with the flow-velocity component of the dia-surface transport term that  
 324 appears in the mass budget equation (15),

$$\int_{\mathcal{A}_{\mathcal{R}}(\tilde{\lambda}, t)} \rho \mathbf{v} \cdot \frac{\nabla\lambda}{|\nabla\lambda|} dS = \int_{\mathcal{A}_{\mathcal{R}}(\tilde{\lambda}, t)} \rho \mathbf{v} \cdot \mathbf{n}^{(\tilde{\lambda})} dS. \quad (18)$$

325 The boundary-velocity component of the dia- $\tilde{\lambda}$  transport term is instead defined kine-  
 326 matically as the velocity  $\mathbf{v}^{(\lambda)}$  along which  $\lambda$  is materially conserved,

$$\frac{\partial\lambda}{\partial t} + \mathbf{v}^{(\lambda)} \cdot \nabla\lambda = 0. \quad (19)$$

327 Again assuming  $|\nabla\lambda| \neq 0$ , equation (19) can be multiplied by  $\rho/\nabla\lambda$  and rearranged  
 328 as

$$\rho \mathbf{v}^{(\lambda)} \cdot \hat{\mathbf{n}}^{(\lambda)} = -\frac{\rho}{|\nabla\lambda|} \frac{\partial\lambda}{\partial t}. \quad (20)$$

329 Substituting equations (18) and (20) into equation (17), we can re-express the dia- $\tilde{\lambda}$  mass  
 330 transport in terms of isosurface-integrated  $\lambda$ -tendencies, evaluated along the particular  
 331  $\lambda = \tilde{\lambda}$  isosurface,

$$\int_{\mathcal{A}_{\mathcal{R}}(\tilde{\lambda}, t)} \rho (\mathbf{v} - \mathbf{v}^{(\tilde{\lambda})}) \cdot \hat{\mathbf{n}}^{(\tilde{\lambda})} dS = \int_{\mathcal{A}_{\mathcal{R}}(\tilde{\lambda}, t)} \rho \frac{(\frac{\partial\lambda}{\partial t} + \mathbf{v} \cdot \nabla\lambda)}{|\nabla\lambda|} dS = \int_{\mathcal{A}_{\mathcal{R}}(\tilde{\lambda}, t)} \frac{\rho \dot{\lambda}}{|\nabla\lambda|} dS. \quad (21)$$

332 To make evaluation of the surface integrals in equation (21) more amenable to our  
 333 anticipated finite-volume discretization, we reformulate the definition of  $\lambda$ -water masses  
 334 as integrals in  $\lambda$  coordinates. Applying the chain rule, we first re-express the dia- $\lambda$  thick-  
 335 ness,  $dh$ , of an infinitesimal volume element  $dV$  in  $\lambda$  coordinates,  $d\lambda = |\nabla\lambda| dh$ , such  
 336 that  $dV = dh dS = d\lambda dS/|\nabla\lambda|$ . We can re-express the density-weighted integral of  
 337 an arbitrary scalar function  $\mathcal{F}(\mathbf{x}, t)$  over the water mass  $\Omega(\tilde{\lambda}, t)$  as

$$G_{\Omega}^{(\mathcal{F})}(\tilde{\lambda}, t) \equiv \int_{\Omega(\tilde{\lambda}, t)} \rho \mathcal{F} dV = \int_{-\infty}^{\tilde{\lambda}} \left[ \oint_{\mathcal{A}_{\mathcal{R}}(\tilde{\lambda}', t)} \rho \mathcal{F} dS \right] dh = \int_{-\infty}^{\tilde{\lambda}} \left[ \oint_{\mathcal{A}_{\mathcal{R}}(\tilde{\lambda}', t)} \frac{\rho \mathcal{F}}{|\nabla\lambda|} dS \right] d\tilde{\lambda}', \quad (22)$$

338 where we emphasize that  $\partial\Omega(\tilde{\lambda}, t)$  is the full boundary of the water mass while  $\mathcal{A}_{\mathcal{R}}(\tilde{\lambda}, t)$   
 339 is just the  $\tilde{\lambda}$ -isosurface and excludes the lateral boundary  $\partial\mathcal{R}$  and the seafloor. Taking

340 the partial derivative with respect to  $\tilde{\lambda}$  and applying the Fundamental Theorem of Cal-  
 341 culus, we have the generalized *dia- $\tilde{\lambda}$  transformation relation* for the arbitrary scalar  $\mathcal{F}$ ,

$$\mathcal{G}_{\Omega}^{(\mathcal{F})}(\tilde{\lambda}, t) \equiv \partial_{\tilde{\lambda}} G_{\Omega}^{(\mathcal{F})} = \partial_{\tilde{\lambda}} \left[ \int_{\Omega(\tilde{\lambda}, t)} \rho \mathcal{F} dV \right] = \oint_{\mathcal{A}_{\mathcal{R}}(\tilde{\lambda}, t)} \frac{\rho \mathcal{F}}{|\nabla \lambda|} dS. \quad (23)$$

342 In doing so, we have ignored the contribution from the lower bound ( $\tilde{\lambda}' \rightarrow -\infty$ ) be-  
 343 cause  $\int_{\mathcal{A}_{\mathcal{R}}(\tilde{\lambda}', t)} \frac{\rho \mathcal{F}}{|\nabla \lambda|} dS \rightarrow 0$  as  $\tilde{\lambda}'$  decreases below the range of realizable values and thus  
 344 the area  $\mathcal{A}_{\mathcal{R}}(\tilde{\lambda}', t)$  of the isosurface vanishes; in practice, it suffices to set a lower limit  
 345 of  $\tilde{\lambda}_0 < \min\{\lambda(\mathbf{x}, t)\}$ .

346 Taking the arbitrary scalar  $\mathcal{F}$  to be  $\lambda$ -tendencies, the dia- $\tilde{\lambda}$  transformation rela-  
 347 tion (23) allows us to express the surface integrals in equation (21) as volume integrals.  
 348 First, we integrate the density-weighted  $\lambda$  conservation equation (17) over  $\Omega(\tilde{\lambda}, t)$  and  
 349 take a derivative with respect to  $\tilde{\lambda}$ :

$$\underbrace{\frac{\partial}{\partial \tilde{\lambda}} \left[ \int_{\Omega(\tilde{\lambda}, t)} \rho \frac{\partial \lambda'}{\partial t} dV \right]}_{\mathcal{G}_{\Omega}^{(\partial_t)}(\tilde{\lambda}, t)} + \underbrace{\frac{\partial}{\partial \tilde{\lambda}} \left[ \int_{\Omega(\tilde{\lambda}, t)} \rho (\mathbf{v} \cdot \nabla \lambda') dV \right]}_{\mathcal{G}_{\Omega}^{(A)}(\tilde{\lambda}, t)} = \frac{\partial}{\partial \tilde{\lambda}} \left[ \int_{\Omega(\tilde{\lambda}, t)} \rho \dot{\lambda}' dV \right]. \quad (24)$$

350 We refer to equation (24) as the  $\lambda$ -*Water Mass Transformation* ( $\lambda$ -WMT) equation be-  
 351 cause the dia- $\tilde{\lambda}$  transformation relation (23) allows us to then combine equations (21)  
 352 and (24), yielding an expression for the dia- $\tilde{\lambda}$  transport in terms of differential  $\lambda$ -transformation  
 353 tendencies integrated over the water mass (see definition on RHS of equation 24),

$$\int_{\mathcal{A}_{\mathcal{R}}(\tilde{\lambda}, t)} \rho (\mathbf{v} - \mathbf{v}(\tilde{\lambda})) \cdot \hat{\mathbf{n}}(\tilde{\lambda}) dS = \mathcal{G}_{\Omega}^{(T)}(\tilde{\lambda}, t), \quad (25)$$

354 which we simply refer to as the total *water mass transformation*. The terms in equations  
 355 (24) and (25) have units of mass transport, kg/s; motivated by the Boussinesq approx-  
 356 imation, they can be converted into equivalent volume transports (units of  $\text{m}^3/\text{s}$  or  $\text{Sv} \equiv$   
 357  $10^6 \text{ m}^3/\text{s}$ ) by dividing by a reference density such as  $\rho_0 \approx 1035 \text{ kg}/\text{m}^3$ .

358 Now that we have defined our final expressions for each term, we drop the variables'  
 359 arguments for conciseness. It is often useful to decompose the transformation term by  
 360 process type (Figure 2), e.g.,

$$\mathcal{G}_{\Omega}^{(T)} \equiv \mathcal{G}_{\Omega}^{(\text{Surface})} + \mathcal{G}_{\Omega}^{(\text{Ice-Ocean})} + \mathcal{G}_{\Omega}^{(\text{Seafloor})} + \mathcal{G}_{\Omega}^{(\text{Mix})}, \quad (26)$$

361 or even more granularly by physical process (e.g., brine rejection, radiative cooling, di-  
 362 apycnal mixing by internal wave breaking, isopycnal mixing by mesoscale eddies). To  
 363 simplify discussions of the  $\lambda$ -water mass budgets diagnosed from our Baltic Sea simu-  
 364 lation, we hereafter bundle all fluxes across external ocean boundaries into:

$$\mathcal{G}_{\Omega}^{(\text{BF})} \equiv \mathcal{G}_{\Omega}^{(\text{Surface})} + \mathcal{G}_{\Omega}^{(\text{Ice-Ocean})} + \mathcal{G}_{\Omega}^{(\text{Seafloor})}. \quad (27)$$

## 365 2.4 The $\lambda$ -Water Mass Transformation Budget

366 The power of the  $\lambda$ -water mass budget approach arises when we replace the total  
 367 surface integral in the  $\lambda$ -water mass budget equation (8) with our expressions for the nonzero  
 368 mass transports across the sea surface (11), interior  $\tilde{\lambda}$ -isosurfaces (25), and lateral bound-  
 369 aries (14), yielding the concise  $\lambda$ -WMT budget:

$$\partial_t \mathcal{M}_{\Omega} = \mathcal{S}_{\Omega} - \mathcal{G}_{\Omega}^{(T)} + \Psi_{\partial \mathcal{R}}. \quad (28)$$

370 Rearranging equation (28) as

$$\partial_t \mathcal{M}_\Omega - \mathcal{S}_\Omega - \Psi_{\partial\mathcal{R}} = -\mathcal{G}_\Omega^{(T)} \quad (29)$$

371 clarifies the distinction between the *kinematic mass budget terms* on the LHS and the  
 372 *water mass transformation processes* on the RHS. In the context of numerical ocean mod-  
 373 els, equation (29) is not necessarily closed because additional *spurious* water mass trans-  
 374 formations  $\mathcal{G}_\Omega^{(S)}$  can arise due to discretization errors; we defer a detailed investigation  
 375 of spurious numerical mixing until Section 3.5. The  $\lambda$ -WMT budget is illustrated schemat-  
 376 ically in Figure 2.

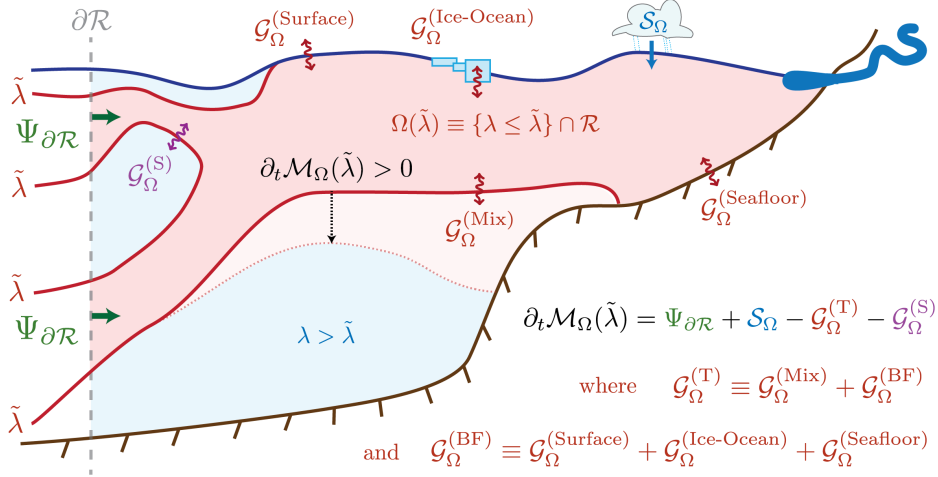


**Figure 2.** A schematic  $(x, z)$  profile view of the  $\lambda$ -WMT budget (equation (41)) for a water mass  $\Omega(\tilde{\lambda}, t)$  defined by the region  $\mathcal{R}$  and tracer values that satisfy  $\lambda(\mathbf{x}, t) \leq \tilde{\lambda}$  for a specific choice of  $\tilde{\lambda}$ . Note that  $\lambda$  is not required to be monotonic with depth and it is possible for multiple isosurfaces of  $\lambda$  to exist within a single vertical profile. The water mass  $\Omega(\tilde{\lambda}, t)$  is bounded by the seafloor (brown), sea surface (blue), interior  $\lambda$ -isosurfaces (red), and a specified regional boundary  $\partial\mathcal{R}$  (grey dashed). The various terms in the budget are defined throughout Section 2. The dia-scalar transformation term  $\mathcal{G}_\Omega^{(T)}$  is decomposed into the contributions from fluxes across the sea surface, seafloor, and  $\lambda$ -isosurface. An additional term  $\mathcal{G}_\Omega^{(S)}$  is introduced to account for water mass transformations associated with spurious numerical mixing (see Section 3.5).

## 377 2.5 Example: Water Mass Transformations in the Baltic Sea

378 Example evaluations of the  $\lambda$ -WMT budget equation (29) are shown in Figure 3  
 379 for  $\lambda = \Theta$  (Conservative Temperature),  $S$  (Absolute Salinity), and  $\rho_0$  (potential density  
 380 referenced to atmospheric pressure) in a region  $\mathcal{R}$  of the inner Baltic Sea (whose bound-  
 381 ary  $\partial\mathcal{R}$  is visualized later in Figures 5 and 9). The region contains two distinct water  
 382 masses (Figure 3a): (1) light fresh water of seasonally-varying temperature in the shal-  
 383 low inner Baltic Sea and (2) salty, cold, and dense open ocean water at the entrance to  
 384 the Baltic Sea. Let us consider the dominant features of this region's annual-mean WMT  
 385 budgets.

386 In temperature space (Figure 3b), a leading-order balance emerges between sur-  
 387 face heat fluxes (which warm warm water and cool cold water) and interior mixing (which  
 388 mixes cold and warm waters together, transforming both towards intermediate temper-  
 389 atures). Interestingly, near  $2.5^\circ\text{C}$ , the warming of cold waters due to mixing is not bal-  
 390 anced by surface cooling, resulting in a small annual mean drift towards warmer water

391 classes. In salinity space (Figure 3c), we see two distinct lobes of water mass transfor-  
 392 mation, consistent with the bimodal water mass distribution seen in Figure 3a. For the  
 393 deep water lobe with  $S > 20$  ppt, interior mixing again produces a straightforward dipole  
 394 structure as relatively fresh ( $S < 29$  ppt) and salty ( $> 29$  ppt) waters are mixed together;  
 395 however, only the fresh part of these mixing-driven transformations are balanced by sur-  
 396 face flux salinification, with the freshening of the salty part instead being primarily bal-  
 397 anced by a net export of relatively fresh water into the open ocean. The WMT budget  
 398 in potential density space (Figure 3d) closely follows that of salinity, except for the light-  
 399 est waters ( $\rho_0 < 1007 \text{ kg/m}^3$ ) where the temperature-related transformations are con-  
 400 centrated.

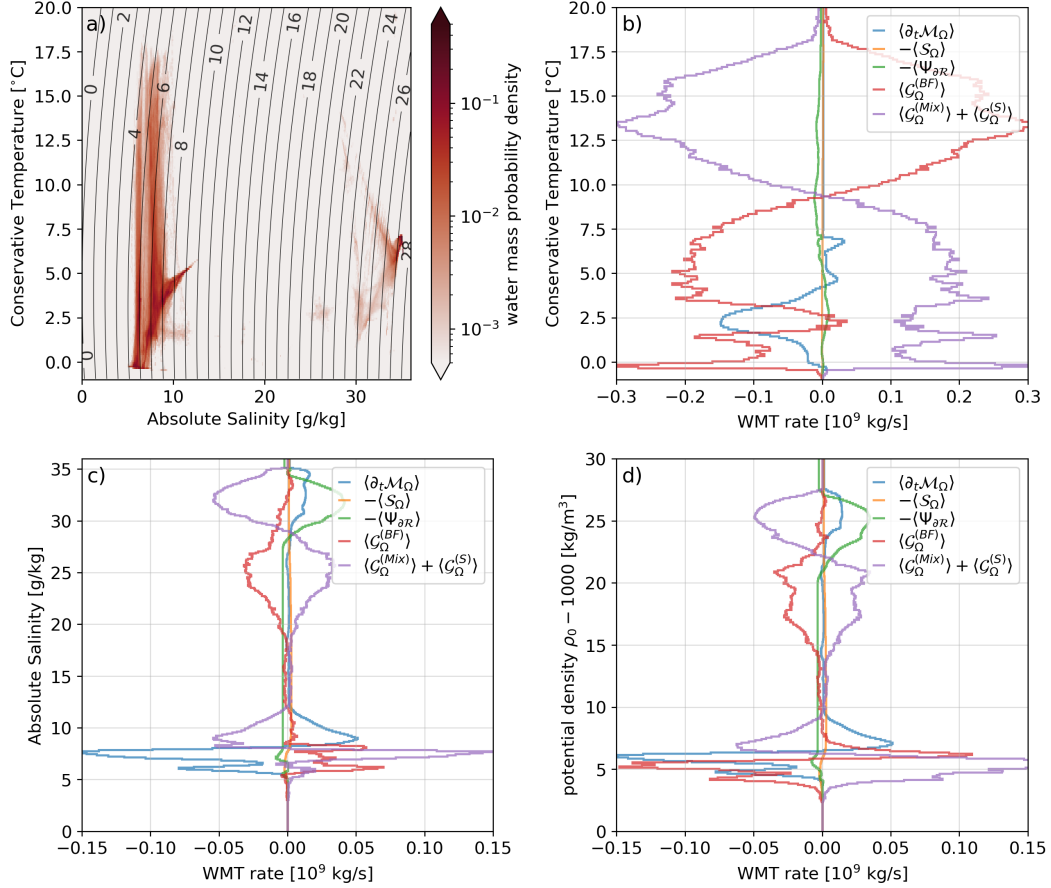


**Figure 3.** Examples of water masses and their budgets for the region  $\mathcal{R}$  of the Baltic Sea shown in Figure 9. a) The distribution of water masses in  $\mathcal{R}$  as a function of Conservative Temperature, Absolute Salinity, and potential density  $\rho_0 - 1000 \text{ kg/m}^3$  (referenced to atmospheric pressure, shown as black contours) averaged over a full year, mainly provided as context for the budgets that follow. b-d) Annual-mean (angle brackets) WMT budgets (eq. 29) in Conservative Temperature, Absolute Salinity, and potential density coordinates, diagnosed as described in Section 3 but using timestep-averaged diagnostics in the model’s native prognostic vertical coordinate to minimize discretization errors. Total water mass transformations  $\mathcal{G}_\Omega^{(T)}$  are broken down into two components: boundary fluxes  $\mathcal{G}_\Omega^{(BF)}$  and mixing, which includes both directly diagnosed parameterized mixing  $\mathcal{G}_\Omega^{(Mix)}$  and spurious numerical mixing  $\mathcal{G}_\Omega^{(S)}$ , which we identify as the remainder of the other budget terms (see Section 3.5). With in-situ densities of  $\rho \approx 1000 \text{ kg/s}$ , a water mass transformation rate of  $10^9 \text{ kg/s}$  is approximately equivalent to  $1 \text{ Sv} \equiv 10^6 \text{ m}^3/\text{s}$ .

401

## 2.6 On steady-state $\lambda$ -Water Mass Transformation Budgets

402

403

Assuming a steady-state (i.e.  $\mathbf{v}^{(\tilde{\lambda})} = 0$ ) and neglecting the typically small surface mass flux term (i.e.  $\mathcal{S}_\Omega = 0$ ), the WMT budget equations (15 and 29) reduce to:

$$\Psi_{\partial\mathcal{R}} = \int_{\mathcal{A}_{\mathcal{R}}(\tilde{\lambda})} \rho \mathbf{v} \cdot \hat{\mathbf{n}}^{(\tilde{\lambda})} dS = \mathcal{G}_\Omega^{(T)}. \quad (30)$$

404

405

406

407

408

409

410

411

412

413

414

415

416

417

We remind the reader that the area  $\mathcal{A}_{\mathcal{R}}(\tilde{\lambda})$  of the  $\tilde{\lambda}$ -isosurface within  $\mathcal{R}$  is the subset of the total water mass boundary  $\partial\Omega$  that excludes the lateral boundary  $\partial\mathcal{R}$ , the sea surface, and the seafloor. Equation (30) states that the convergent horizontal circulation into a region is exactly balanced by the circulation across its bounding  $\tilde{\lambda}$ -isosurface, which is driven by the sum of the water mass transformation processes. A common application of water mass transformation theory is to use an estimate of the RHS of the steady-state equation (30) in density coordinates to infer the diapycnal overturning circulation it induces on the LHS (e.g. de Lavergne et al., 2016; Ferrari et al., 2016; Drake et al., 2020). Marsh et al. (2000) warn, however, about the dangers of incorrectly applying the steady state equation (30) to an unsteady meridional overturning circulation. Testing the steady-state assumption in the context of our annual-mean S-WMT budgets in the Baltic Sea (Figure 4), we find that the assumption is fairly reasonable for salty waters (in the deep open ocean), but not the fresh waters (in the shallow inner Baltic Sea) which are drifting at leading order (Figure 3c).

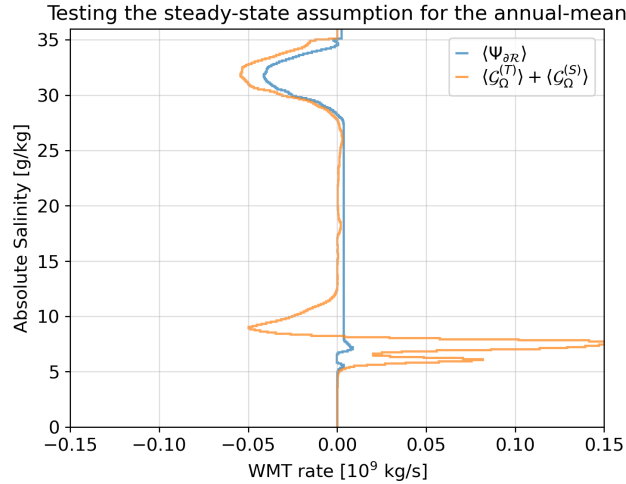


**Figure 4.** A test of the steady-state S-WMT budget assumption (eq. 30), reproducing Figure 3c except that we have now bundled all of the transformation terms together, including both directly diagnosed transformations  $\mathcal{G}_\Omega^{(T)} = \mathcal{G}_\Omega^{(\text{BF})} + \mathcal{G}_\Omega^{(\text{Mix})}$  and spurious transformations  $\mathcal{G}_\Omega^{(S)}$  (see Section 3.5) and have changed the sign of the transport term for more direct comparison.

418

## 3 Diagnosing Discretized $\lambda$ -Water Mass Transformation Budgets

419

420

421

In this section, we adapt the continuous theory outlined above to express the WMT budget in a form befitting the diagnostic output provided by numerical ocean models. We would like to diagnose the terms in the time-mean WMT budget (29), given by

$$\langle \partial_t \mathcal{M}_\Omega \rangle - \langle \mathcal{S}_\Omega \rangle - \langle \Psi_{\partial\mathcal{R}} \rangle + \langle \mathcal{G}_\Omega^{(T)} \rangle = 0 \quad (31)$$

422 where

$$\langle \phi \rangle \equiv \frac{1}{\Delta t} \int_{t_n}^{t_n+\Delta t} \phi dt \quad (32)$$

423 is the diagnostic time-averaging operator over a given interval of length  $\Delta t$  and centered  
 424 around  $t_{n+\frac{1}{2}}$ . For clarity, we assume *a priori* that all diagnostics have been conserva-  
 425 tively regridded and remapped into  $\lambda$  bins  $[\lambda_{m-\frac{1}{2}}, \lambda_{m+\frac{1}{2}}]$  (denoting layer  $m$ ), where over-  
 426 bars  $\overline{\phi}^m$  denote layer averages. We emphasize that whatever vertical regridding/remapping  
 427 scheme is employed, it should be conservative so that total water mass and tracer con-  
 428 tent is conserved. Any any case, results should be robust to changes in the diagnostic  
 429 and target grids (see Section 3.6). We will use  $i$  and  $j$  as horizontal grid indices (with  
 430 a straightforward extension to adjacency matrices for unstructured mesh implementa-  
 431 tions, e.g. Ringler et al. (2013)) and  $q$  as the  $\lambda$  layer index. We discuss aliasing errors  
 432 due to ‘offline’ remapping with time-mean diagnostics in Section 3.6.

### 433 3.1 Kinematic mass tendency

434 The Fundamental Theorem of Calculus allows us to write the time-mean mass ten-  
 435 dency term as the difference between snapshots bounding the averaging interval,

$$\langle \partial_t \mathcal{M}_\Omega \rangle = (\Delta t)^{-1} [\mathcal{M}_\Omega]_{t_n}^{t_n+\Delta t}. \quad (33)$$

436 For a given interface  $\tilde{\lambda} = \lambda_{m+\frac{1}{2}}$ , each of these mass snapshots can be estimated by cu-  
 437 mulatively summing layer masses,  $h_q \overline{\rho}^q dA$ , for all layers with  $\lambda_q \leq \lambda_{m+\frac{1}{2}}$  within a tracer  
 438 cell mask  $R$  that approximates the continuous region  $\mathcal{R}$ ,

$$\langle \partial_t \mathcal{M}_\Omega \rangle (\lambda_{m+\frac{1}{2}}, t_{n+\frac{1}{2}}) \simeq \frac{1}{\Delta t} \left[ \sum_{i,j \in R} \sum_{q < m+\frac{1}{2}} h_q \overline{\rho}^q dA \right]_{t_n}^{t_n+\Delta t}. \quad (34)$$

### 439 3.2 Convergent horizontal mass transport

440 The transport term,  $\langle \Psi_\Omega \rangle$ , requires accumulating all mass transports normal to the  
 441 region’s boundary,  $\partial R$ , with a consistently convergent orientation, for  $\lambda \leq \tilde{\lambda}$ . Since the  
 442 surface integral form of this term originates from the divergence theorem, internal con-  
 443 sistency of the discretized mass budget requires that the discrete boundary,  $\partial R \approx \partial \mathcal{R}$ ,  
 444 exactly follow the faces of the finite volume elements that bound the tracer cell mask,  
 445  $R$ , as illustrated in Figure 5. The total convergent transport across  $\partial R$  is computed by  
 446 summing the convergent mass transports over all layers with  $\lambda_q \leq \lambda_{m+\frac{1}{2}}$  and over all  
 447 of the cell faces along the boundary  $\partial R$ :

$$\langle \Psi_{\partial R} \rangle (\lambda_{m+\frac{1}{2}}, t_{n+\frac{1}{2}}) \equiv \left\langle \int_{\partial R \cap \{\lambda \leq \lambda_{m+\frac{1}{2}}\}} -\rho \mathbf{u} \cdot \hat{\mathbf{n}}^{(\partial R)} dA \right\rangle \simeq \sum_{i^{(\mathbf{u})}, j^{(\mathbf{u})} \in \partial R} \left[ \sum_{\lambda_q \leq \lambda_{m+\frac{1}{2}}} (-\overline{\rho}^q h_q d\ell) \cdot \hat{\mathbf{n}}^{(\partial R)} \right], \quad (35)$$

448 where  $i^{(\mathbf{u})}, j^{(\mathbf{u})}$  are the grid face indices that correspond to the normal mass fluxes  $[(\rho \mathbf{u}) \cdot \hat{\mathbf{n}}^{(\partial R)}] \hat{\mathbf{n}}^{(\partial R)}$   
 449 and  $d\ell$  are the widths of grid cell faces. Since local recirculations can be orders of mag-  
 450 nitude larger than the net convergence into a region (Figure 5, inset arrows), inexact in-  
 451 terpolation methods (e.g. for a boundary  $\partial R$  that does not exactly follow the grid cell  
 452 faces bounding the mask  $R$ ) or seemingly minor indexing errors can balloon into leading-  
 453 order errors in the overall WMT budget and therefore corrupt the identification of the  
 454 residual as spurious numerical mixing.

455 Our method for directly computing boundary-normal convergent transports, which  
 456 consists of finding pairs of grid face indices ( $i^{(\mathbf{u})}, j^{(\mathbf{u})}$ ) and assigning the appropriate sign  
 457 for the inward orientation  $-(\overline{\rho}^q h_q d\ell) \cdot \hat{\mathbf{n}}^{(\partial R)}$ , is illustrated in Figure 5 and briefly de-  
 458 scribed in Appendix D. We have verified for various definitions of discrete boundaries

459  $R \approx \mathcal{R}$  that the surface integral of the convergent mass flux along  $\partial R$  is within machine  
 460 precision of the volume-integrated convergent mass flux diagnostic within  $R$ , thereby sat-  
 461 isfying the divergence theorem on the model grid.

462 An alternative method of diagnosing the convergent horizontal mass transport into  
 463 the discrete region  $R$  is to first compute the convergence into each individual grid col-  
 464 umn  $C$  (where  $R = \bigcup\{C\}$ ), and then sum the convergent transport over all of the columns  
 465 in  $R$  to get the net convergent transport,

$$\langle \Psi_{\partial R} \rangle(\lambda_{m+\frac{1}{2}}, t_{n+\frac{1}{2}}) \simeq \sum_{C \subseteq R} \left\{ \sum_{i(\mathbf{u}), j(\mathbf{u}) \in \partial C} \left[ \sum_{\lambda_q \leq \lambda_{m+\frac{1}{2}}} (\bar{\rho} \mathbf{u}^q h_q d\ell) \cdot \hat{\mathbf{n}}^{(\partial C)} \right] \right\}. \quad (36)$$

466 [We use this approach to diagnose the maps of column-wise horizontal mass transport  
 467 convergence shown in Figure 9c, discussed in detail later in the text]. Benefits of com-  
 468 puting the convergence of horizontal mass transports for each grid column individually  
 469 are: 1) it is readily diagnosed from the finite difference of horizontal mass transports across  
 470 the lateral faces of a grid column, significantly simplifying its implementation; 2) it is  
 471 positioned at the center of tracer grid cells, allowing it to be conveniently integrated with  
 472 all of the other diagnostics required to close the  $\lambda$ -WMT budget; 3) it can be precom-  
 473 puted once globally and then efficiently reused for various choices of  $R$ ; and 4) it enables  
 474 column-wise estimation of spurious numerical mixing (see Section 3.5 and Holmes et al.  
 475 (2021)), rather than a single bulk estimate for the entire region  $R$ . A major disadvan-  
 476 tage of this column-wise approach, however, is that it provides no information about the  
 477 spatial structure of normal mass transports along the boundary  $\partial R$  (as shown in Fig-  
 478 ure 5), which may be necessary information for some applications. Our software pack-  
 479 ages described in Appendix D allow users to specify either of these two methods to cal-  
 480 culate the transport convergence term.

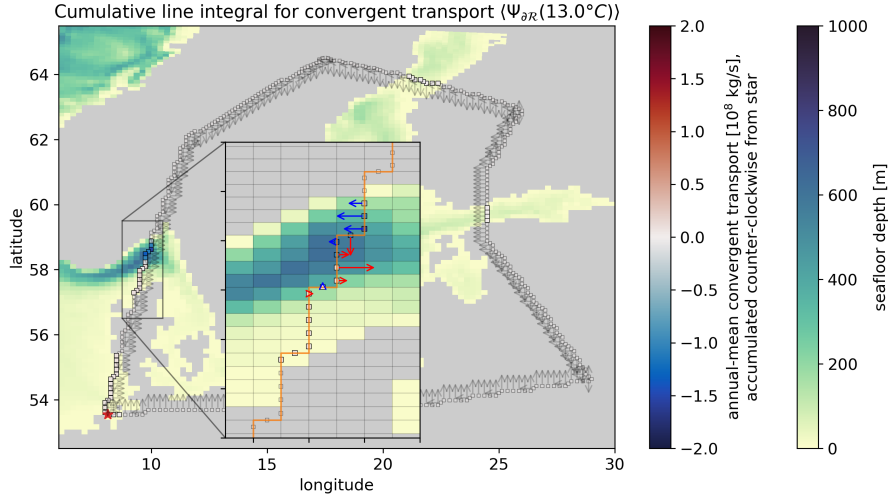


**Figure 5.** Annual-mean convergent transport (expression 36 diagnosed as 35) into the discrete region  $R$ , integrated for waters colder than  $\Theta = 13^\circ\text{C}$ , as a counterclockwise cumulative line integral beginning from the red star. The black arrows show the orientation of the inward-facing normal vectors  $-\hat{\mathbf{n}}^{(\partial R)}$  for each grid face along the discrete boundary  $\partial R$ . The inset zooms in on the entrance to the Baltic Sea, where the net mass transport is the relatively small residual of fluxes in (red arrows) and out (blue arrows) of the region; for clarity, we only show the handful of arrows that correspond to transports larger than 10% of the maximum cross-boundary transport.

### 3.3 Boundary mass source

The boundary mass source term,

$$\langle \mathcal{S}_\Omega \rangle (\lambda_{m+\frac{1}{2}}, t_{n+\frac{1}{2}}) = \left\langle \int_{\partial\Omega_{\text{surf}}} Q_M^{\text{surf}} dA \right\rangle, \quad (37)$$

is estimated by simply summing  $Q_M^{\text{surf}} dA$  for all  $\lambda_q^{\text{surf}} \leq \lambda_{m+\frac{1}{2}}$ . This term is globally small but can be important in smaller regions with large and concentrated freshwater fluxes (e.g. major river inflows or rapidly melting sea ice, icebergs, or ice shelves).

### 3.4 Transformation rates

Water mass transformation terms  $\mathcal{G}_\Omega^{(*)}$ , i.e. those in the form of the  $\lambda$ -Water Mass Transformation equation (24), are approximated by finite difference:

$$\mathcal{G}_\Omega^{(T)} \equiv \frac{\partial}{\partial \bar{\lambda}} \int_{\Omega(\bar{\lambda}, t)} \rho \dot{\lambda} dV \simeq \frac{\int_{\Omega(\lambda_{m+\frac{1}{2}})} \rho \dot{\lambda} dV - \int_{\Omega(\lambda_{m-\frac{1}{2}})} \rho \dot{\lambda} dV}{\lambda_{m+\frac{1}{2}} - \lambda_{m-\frac{1}{2}}} \quad (38)$$

where  $\rho \dot{\lambda} dV$  represents tracer mass tendencies arising from material transformation processes. In the Riemann sum evaluation of the integral, these tendencies take the form of the density-weighted and layer-integrated tracer tendency terms shown in equations (A34)–(A35) (derived in Appendix A), as scaled by the vertically-uniform area element  $dA$ .

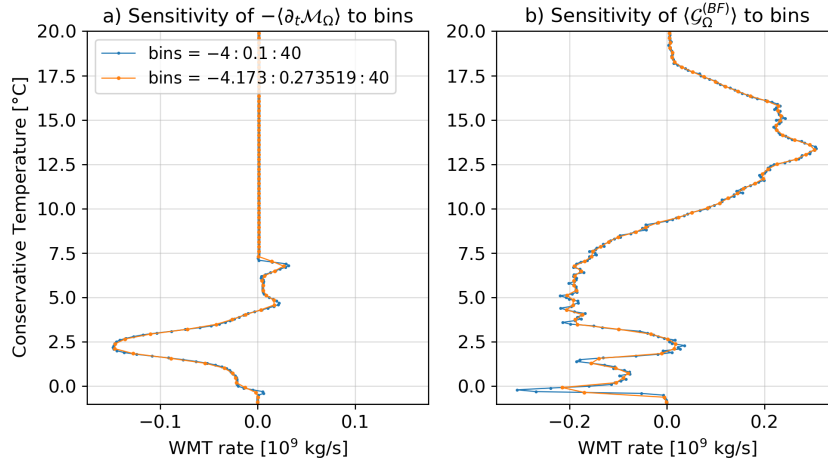


**Figure 6.** Sensitivity of the  $\Theta$ -WMT budget to the choice of  $\lambda$  bins for (a) the mass tendency term and (b) the boundary flux transformation rate term (eq. 27). Both terms are integrated over the discrete region mask  $R$  shown in Figure 5. Blue curves show the default bins (every 0.1 °C, from  $-4$  °C to 40 °C) and orange curves show the same terms recalculated with alternative bins that are larger than, and offset from, the default. Differences between the two calculations are much smaller than the resolved features of interest, giving us confidence that discretization errors in our offline diagnostic methods are negligible.

Water mass transformation rates can be inherently noisy, making it difficult to distinguish actual process-based variability from methodological errors. A robust method for assessing whether variability is due to diagnostic discretization errors is to assess the

497 results' sensitivity to the choice of the target  $\tilde{\lambda}$  bins. For three-dimensional general cir-  
 498 culation models and  $\mathcal{O}(100)$  target bins, it is common for each target bin to represent  
 499 thousands of grid cells and thus for the results to be relatively robust. Regions of excep-  
 500 tionally strong or weak gradients,  $|\nabla\lambda|$ , however, may require more careful considera-  
 501 tions of the target  $\tilde{\lambda}$  grid. Our experience is that sensitivity to binning is sufficiently small  
 502 to not affect interpretation of results (see Figure 6), except perhaps for small regions con-  
 503 sisting of just a few grid columns. Noise at the grid column level was a major motiva-  
 504 tion for Holmes et al. (2021)'s diathermal transport approach, which essentially amounts  
 505 to smoothing out the noise in the  $\Theta$ -WMT budget equation by integrating in  $\Theta$ .

### 506 3.5 Spurious numerical mixing

507 Theoretically, the time-averaged  $\lambda$ -WMT budget (31) should exactly hold (with  
 508 the minor caveat that, strictly speaking, this also requires  $|\nabla\lambda| \neq 0$  along the  $\tilde{\lambda}$ -isosurface).  
 509 In practice, however, discretization errors in the advection schemes used in ocean mod-  
 510 els can induce water mass transformations in excess of those resulting from the imposed  
 511 or parameterized material transformation processes,  $\rho\dot{\lambda}$ . To build intuition about spu-  
 512 rious mixing, consider the limiting case in which  $\mathcal{R}$  is global, such that  $\langle\Psi_{\partial\mathcal{R}}\rangle = 0$ , and  
 513 there are no prescribed mass fluxes or material tracer tendencies, i.e.  $\mathcal{S}_\Omega = 0$  and  $\dot{\lambda} =$   
 514 0 (such that  $\mathcal{G}_\Omega^{(T)} = 0$ ), respectively. In theory, equation (29) should then reduce to  $\partial_t\mathcal{M}_\Omega =$   
 515 0, meaning the  $\lambda$ -water mass distribution should remain exactly as is. [Note that the steady-  
 516 ness of the  $\lambda$ -water mass distribution does not impose any restrictions on the steadiness  
 517 of the flow or tracer fields, which can in principle still be quite turbulent and variable-  
 518 as in the adiabatic eddy simulations of Marques et al. (2022), with  $\lambda = \rho_2$ ]. Most  
 519 advection schemes employed in ocean models result in errors that are dispersive and/or  
 520 diffusive in nature, which in  $\lambda$ -space manifest as spurious water mass transformations,  
 521 i.e.  $\partial_t\mathcal{M}_\Omega(\tilde{\lambda}, t) \neq 0$ . This point applies even to semi-Lagrangian FV-GVC models in  
 522 which the vertical coordinate  $\sigma$  is  $\lambda$  itself (e.g. density transformations in a density co-  
 523 ordinate model), since such approaches must rely on imperfect vertical regridding/remapping  
 524 schemes to accomodate interior dia- $\sigma$  transports. Purely isopycnal coordinate models  
 525 (e.g. stacked shallow water models) are spared from spurious diapycnal mixing by con-  
 526 struction, but are subject to other problems that limit their viability for global climate  
 527 modeling (Fox-Kemper et al., 2019).

528 In the general case, spurious numerical water mass transformations  $\mathcal{G}_\Omega^{(S)}(\tilde{\lambda}, t)$  can  
 529 be identified as the remainder of the  $\lambda$ -WMT budget equation (29),

$$\mathcal{G}_\Omega^{(S)} \equiv [ - (\partial_t\mathcal{M}_\Omega - \mathcal{S}_\Omega - \Psi_{\partial\mathcal{R}}) ] - \mathcal{G}_\Omega^{(T)} \neq 0, \quad (39)$$

530 where the sign convention is chosen to match those of the other material water mass trans-  
 531 formation terms, for example allowing transformations due to parameterized and spu-  
 532 rious mixing to be directly compared. We emphasize that the remainder  $\mathcal{G}_\Omega^{(S)}$  can be nonzero  
 533 even if both the mass and tracer conservation equations are themselves closed in every  
 534 grid cell, because spurious dia- $\tilde{\lambda}$  transformations may be embedded within the diagnosed  
 535 advective  $\lambda$  tendency. Crucially, closure of cell-wise tracer budgets does not imply clo-  
 536 sure of  $\lambda$ -WMT budgets or that spurious mixing is vanishingly small!

537 Because we have already accounted for all non-advective WMTs when subtract-  
 538 ing  $\mathcal{G}_\Omega^{(T)}$  in equation (39), the remaining spurious numerical errors can only be due to  
 539 errors in the tracer advection operator. [An interpretive limitation of this approach is  
 540 that we are unable to distinguish between spurious WMTs due to horizontal vs. verti-  
 541 cal aspects of advection schemes.] It is useful to interpret the transformations  $\mathcal{G}_\Omega^{(A)}$  di-  
 542 agnosed from the advective tracer tendency in equation (24) as the difference of two dis-  
 543 tinct components:

$$\mathcal{G}_\Omega^{(A)} \equiv \mathcal{G}_\Omega^{(D)} - \mathcal{G}_\Omega^{(S)}, \quad (40)$$

544 where  $-\mathcal{G}_\Omega^{(S)}$  represents transformations due to spurious numerical mixing (diagnosed fol-  
 545 lowing eq. 39, with its arbitrary sign chosen to match that of the other material WMT

546 terms) and we identify  $\mathcal{G}_\Omega^{(D)}$  as the yet unknown diascalar mass transport induced by all  
 547 material transformation (including spurious numerical mixing). Since  $\mathcal{G}_\Omega^{(A)}$  is directly di-  
 548 agnosed from the discrete advective tracer operator, we can also indirectly diagnose the  
 549 sum  $\mathcal{G}_\Omega^{(D)} = \mathcal{G}_\Omega^{(A)} + \mathcal{G}_\Omega^{(S)}$ .

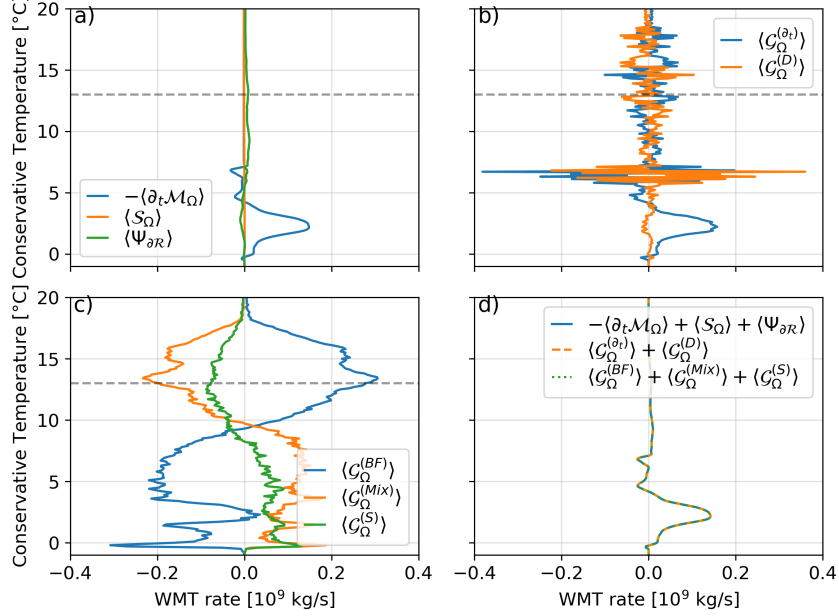


**Figure 7.** Three equivalent ways of decomposing material water mass transformations (equation 41; panel d) in Conservative Temperature coordinates ( $\lambda = \Theta$ ): a) The terms of the kinematic transformation rate; b) the dia-surface transformation rate (which include strongly compensating bin-scale features); and c) the process-based transformation rate, which includes contributions from spurious numerical mixing  $\mathcal{G}_\Omega^{(S)}$  and for which we further decompose the transformation term (following eq. (26)) into boundary flux and interior mixing contributions,  $\mathcal{G}_\Omega^{(T)} = \mathcal{G}_\Omega^{(BF)} + \mathcal{G}_\Omega^{(Mix)}$ . d) Demonstration that all three decompositions are exactly equivalent, which is true by construction because  $\mathcal{G}_\Omega^{(S)}$  and  $\mathcal{G}_\Omega^{(D)}$  are both diagnosed as remainders of the other terms. The inner Baltic Sea region of integration R, is shown in Figure 5. Figure 9 shows the local grid-column contributions to the three key terms for  $\Theta = 13^\circ\text{C}$  (dashed grey line).

550 Combining the definitions (39) and (40) with the water mass transformation equa-  
 551 tion (24), we identify three equivalent and complementary perspectives for interpreting  
 552 water mass change in FV-GVC ocean models:

$$\underbrace{-\partial_t \mathcal{M}_\Omega + \mathcal{S}_\Omega + \Psi_{\partial R}}_{\text{Kinematic transformation}} = \underbrace{\mathcal{G}_\Omega^{(\partial_t)} + \mathcal{G}_\Omega^{(D)}}_{\text{Dia-surface transformation}} = \underbrace{\mathcal{G}_\Omega^{(T)} + \mathcal{G}_\Omega^{(S)}}_{\text{Material property transformation}}. \quad (41)$$

553 The three decompositions of WMT defined by equation 41 are shown in Figure 7. Fig-  
 554 ure 7c shows that spurious numerical mixing plays a large enough role in the budget to  
 555 be non-negligible; its temperature structure closely follows that of parameterized mix-  
 556 ing, but with just 20-50% of its magnitude. Like physical (parameterized turbulent) dif-  
 557 fusion, spurious water mass transformations conserve tracer mass and thus are compen-  
 558 satory in nature, such that the destruction of one water mass is exactly balanced by the  
 559 formation of another.

560 Rearranging equation (7) and decomposing the diagnosed material transformations  
 561 into the components due to boundary fluxes and interior mixing,  $\mathcal{G}_\Omega^{(T)} = \mathcal{G}_\Omega^{(BF)} + \mathcal{G}_\Omega^{(Mix)}$ ,  
 562 we arrive at the closed  $\lambda$ -WMT budget,

$$\partial_t \mathcal{M}_\Omega - \mathcal{S}_\Omega - \Psi_{\partial\mathcal{R}} + \mathcal{G}_\Omega^{(BF)} + \mathcal{G}_\Omega^{(Mix)} + \mathcal{G}_\Omega^{(S)} = 0. \quad (42)$$

563 Figure 8 shows that even when integrated over the many grid columns that comprise the  
 564 inner Baltic region, the  $\Theta$ -WMT budget is highly variable with time. The given isotherm  
 565  $\bar{\Theta} = 13^\circ\text{C}$  only exists in the Baltic region R during the summer, so during the rest of  
 566 the year the water mass  $\Omega$  covers the entire region ( $\Omega = \mathcal{R}$ ) and all of the terms in the  
 567 WMT budget are vanishingly small. During the summer, the budget is dominated by  
 568 the diurnal formation and destruction of cold water masses by boundary heat fluxes (Fig-  
 569 ure 8a). Smoothing over the diurnal cycle, we find that surface heating steadily trans-  
 570 forms cold waters into warmer ones, although this process is partially opposed by pa-  
 571 rameterized mixing with cold waters (Figure 8b). By contrast, in the fall surface fluxes  
 572 and mixing conspire to form cold waters. WMTs due to spurious numerical mixing are  
 573 generally near-zero, but exhibit some short-lived negative excursions that contribute to  
 574 an overall transformation towards lower temperatures—reinforcing the effects of param-  
 575 eterized mixing (Figure 8b). Further smoothing clarifies the annual-mean balance in the  
 576 WMT budget (Figure 8c): net heating by surface fluxes is balanced by parameterized  
 577 and numerical mixing; direct mass fluxes and lateral mass transports into the region are  
 both negligible.

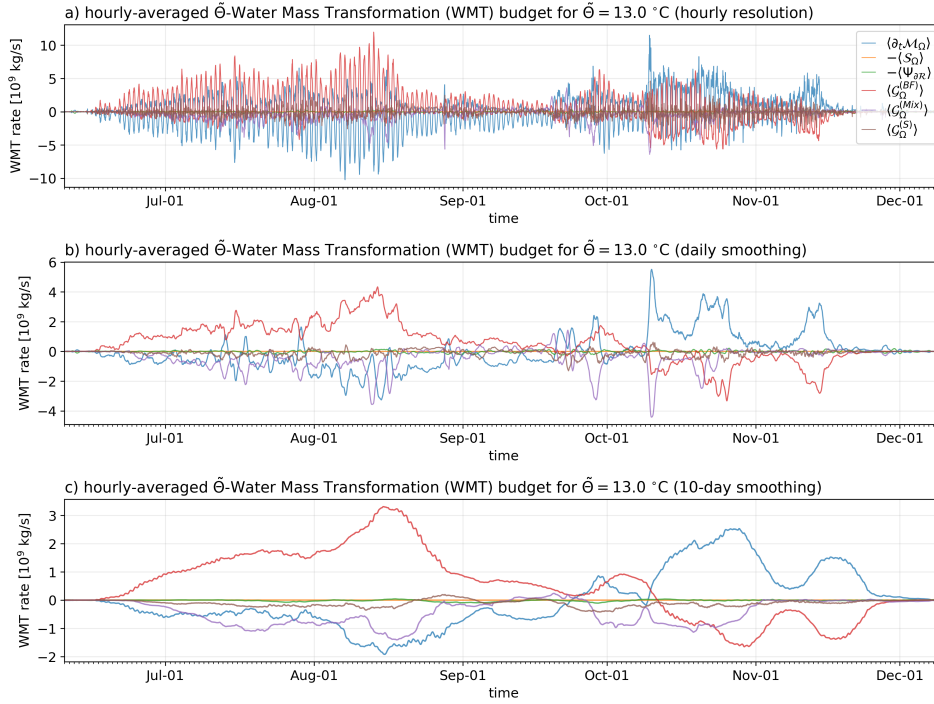


**Figure 8.** Contributions to the  $\Theta$ -WMT budget (eq. 42) integrated over the inner Baltic region, for  $\Theta = 13^\circ\text{C}$ . The hourly (timestep)-averaged budget (a) is dominated by the diurnal cycle, so we also show the results of daily box-averaging (b) and 10-day box-averaging (c).

578

579 It can also be insightful to analyze maps of local (per unit area) WMT rates (e.g.  
 580 Maze et al., 2009; Drake et al., 2020; Holmes et al., 2021). Figure 9 shows the annual-  
 581 mean column-wise WMT budget for waters colder than  $\bar{\Theta} = 13^\circ\text{C}$  in the Baltic region

582 R. The annual-mean mass tendency is small (Figure 9a) because waters warmer than  
 583  $13^\circ\text{C}$  only exist in the summer and the total mass of water columns in the inner Baltic  
 584 does not change much from year to year. The dominant column-wise balance is between  
 585 the warming effect of surface heat fluxes and the cooling effect of parameterized mixing,  
 586 consistent with the region-wide integral. Column-wise lateral mass transport convergence  
 587 and transformations due to spurious numerical mixing are both relatively noisy (Figure  
 588 9a). While the noisy lateral convergent transports average out to near-zero (Figure 8),  
 589 the noisy transformations due to spurious numerical mixing are overwhelmingly nega-  
 590 tive, and contribute to the overall cooling of the water mass.

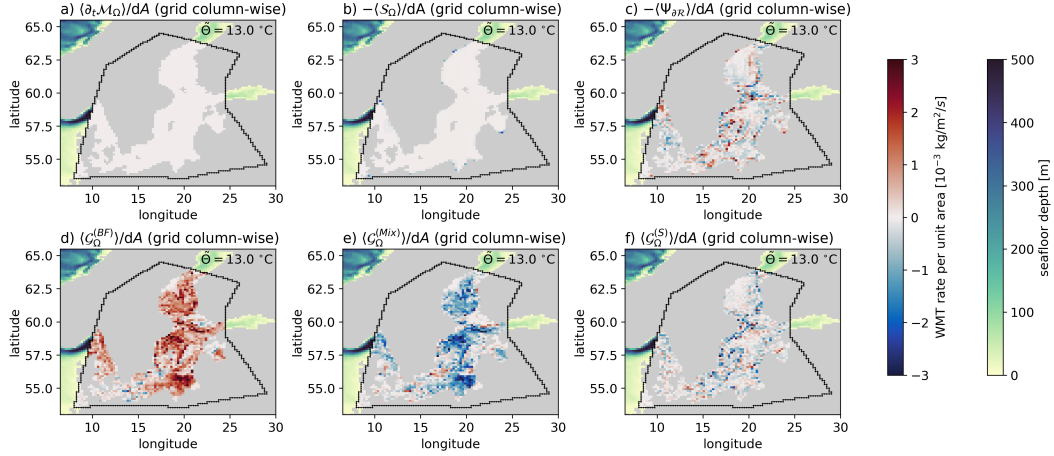


**Figure 9.** Column-wise contributions to the annual-mean  $\Theta$ -WMT budget (eq. 42) by term in the inner Baltic region, for  $\Theta = 13^\circ\text{C}$ . Each panel shows the summand of the corresponding discretized diagnostics described in Section 3, divided by the grid column area  $dA$ . The region  $\mathcal{R}$  is a spherical polygon defined here by the coordinates of eight user-provided vertices, where the black contour shows the discretized boundary  $\partial\mathcal{R}$  that best approximates the continuous boundary  $\partial\mathcal{R}$  as a sequence of model grid faces.

### 591 3.6 Offline vertical remapping and temporal aliasing errors

592 Thus far we have assumed that the required diagnostics are available in  $\lambda$  coordi-  
 593 nates (i.e. were remapped online to a diagnostic grid before time-averaging the outputs).  
 594 In practice, however, one must often make do with diagnostics that are only available  
 595 on other vertical coordinate grids, such as depth levels, isopycnals, terrain-following co-  
 596 ordinates, or other GVCs. Problematically, the time-averaging operator,  $\langle \phi \rangle$ , does not  
 597 commute with vertical remapping if layer-integrated  $\lambda$ -tendencies and  $\lambda$  values covary  
 598 on timescales shorter than the averaging interval. Remapping interval-averaged tracer  
 599 diagnostics to tracer coordinates thereby introduces errors in the WMT budget.

600 In our year-long Baltic Sea test configuration at  $0.25^\circ$  horizontal grid spacing, we  
 601 quantify these errors by brute-force, comparing calculations with diagnostic averaging  
 602 intervals that decrease from monthly, to daily, and finally all the way down to the hourly  
 603 model timestep. First, we consider the sensitivity of the  $\rho_2$ -WMT budget to the diag-  
 604 nostic averaging interval and the choice of vertical coordinate (Figure 10); because  $\rho_2$   
 605 is available as an ‘online’ diagnostic coordinate in our MOM6 simulations,  $\rho_2$ -WMT bud-  
 606 gets are independent of the diagnostic averaging interval (compare Figure 10c,f,i) and  
 607 therefore serve as a ground truth against which we can compare our offline calculations.  
 608 The convergence of the offline depth-level and prognostic hybrid coordinate budgets to-

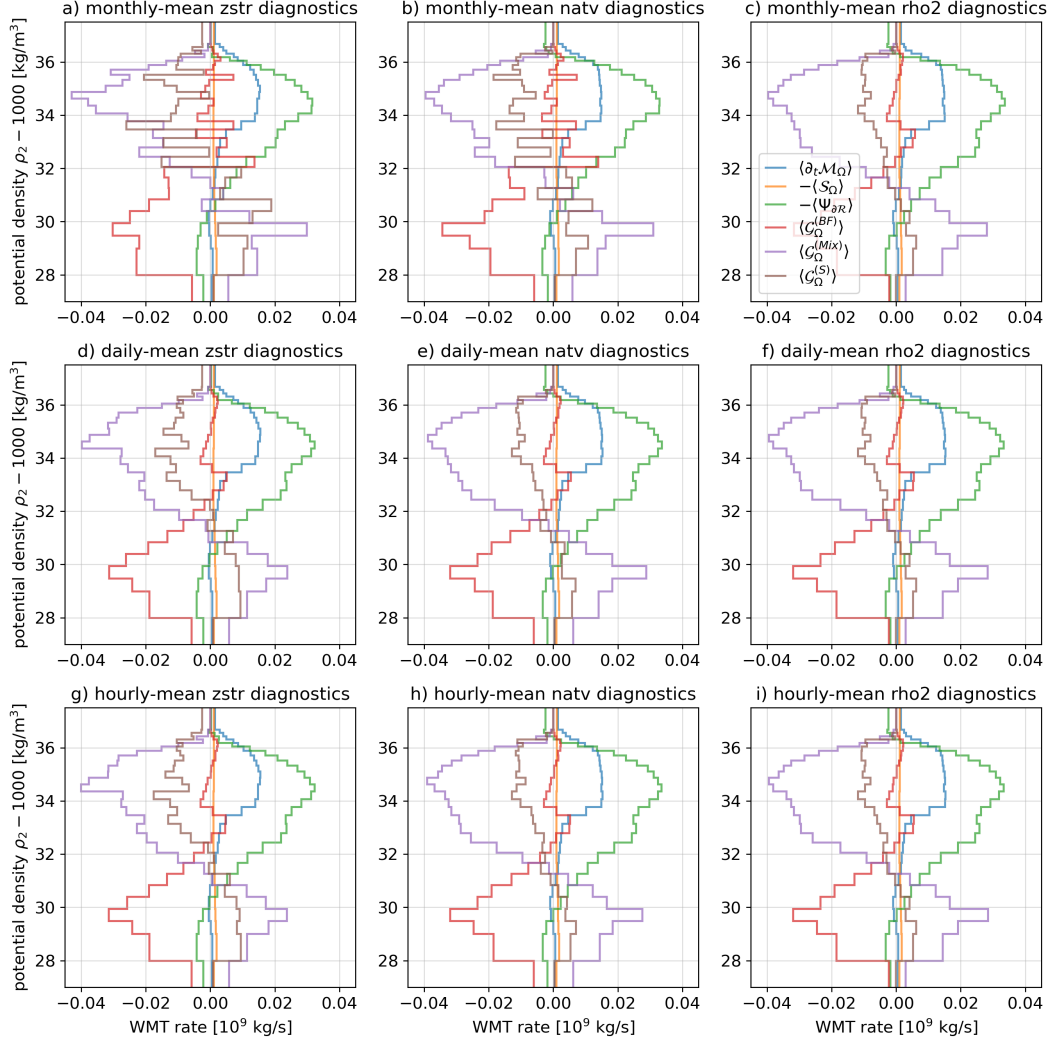


**Figure 10.** Sensitivity of annual-mean  $\rho_2$ -WMT budgets to the diagnostic averaging interval  $\Delta t$  (rows) and the diagnostic vertical coordinate (columns), where **zstr** denotes depth-levels, **natv** denotes prognostic hybrid coordinate levels, and **rho2** denotes potential density surfaces referenced to 2000 dbar. Diagnostics in non-**rho2** coordinates are transformed into the bins of the **rho2** diagnostic to facilitate direct comparison. Because the **rho2** diagnostics are already binned in  $\rho_2$  coordinates online, the WMT budgets for **rho2** are independent of the averaging interval. The non-**rho2** diagnostics converge towards the **rho2** diagnostic results to varying degrees as the averaging interval is reduced; the rate of change and overturning terms are particularly well represented even with monthly-averaged diagnostics.

609 wards the online density coordinate budget (compare 10a-c to d-f to g-i) demonstrates  
 610 that monthly-averaged diagnostics introduce significant errors while daily-mean diagnos-  
 611 tics are nearly indistinguishable from those with the hourly-mean/timestep diagnostics.  
 612 Even with the timestep-averaged diagnostics, however, there are still noticeable errors  
 613 in the **zstr** diagnostics; this is likely because the effective resolution of the **zstr** diag-  
 614 nostic coordinate differs substantially from that of the **natv** and **rho2** diagnostic coordi-  
 615 nates.

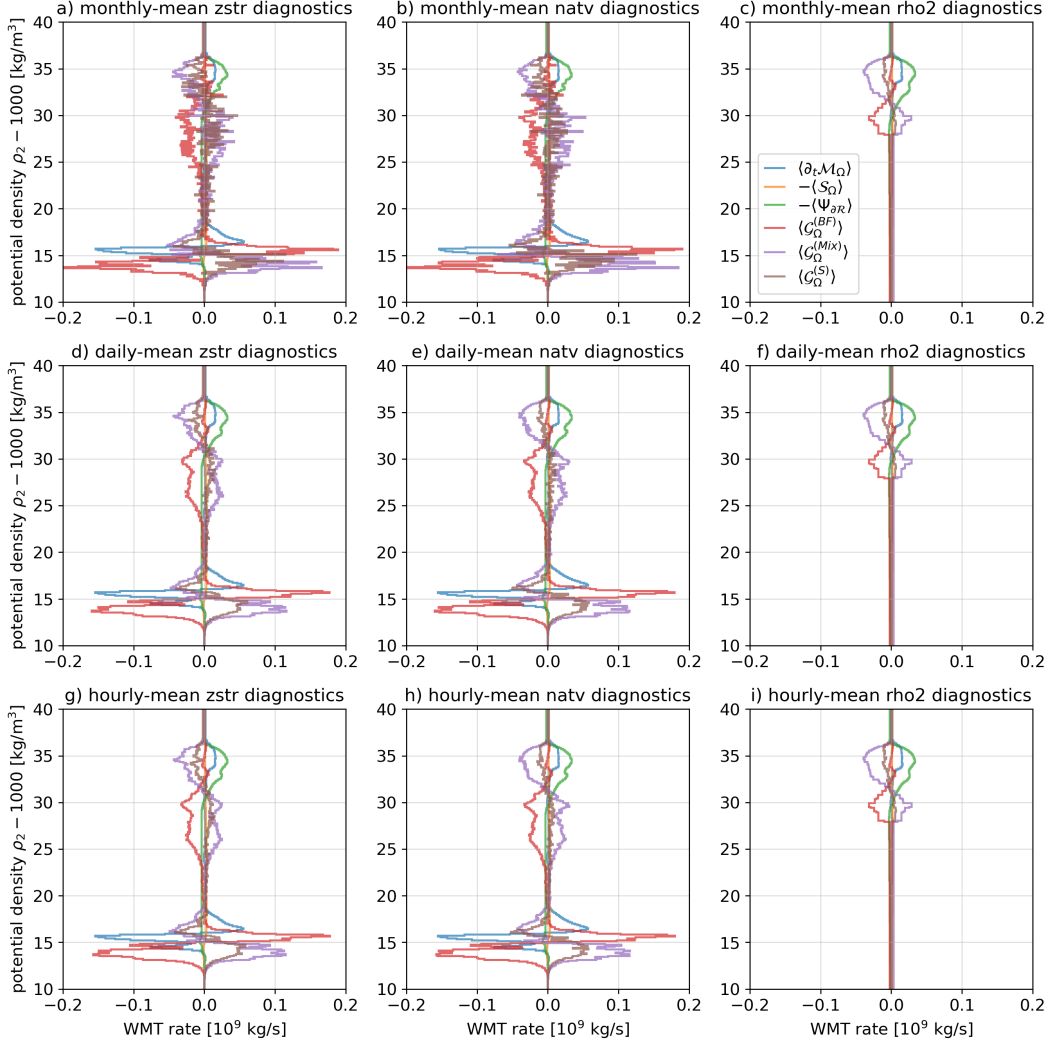


**Figure 11.** Sensitivity of annual-mean  $\rho_2$ -WMT budgets to the diagnostic averaging interval  $\Delta t$  (rows) and the diagnostic vertical coordinate (columns), where **zstr** denotes depth-levels, **natv** denotes prognostic hybrid coordinate levels, and **rho2** denotes potential density surfaces referenced to 2000 dbar. Diagnostics in all three coordinates are transformed into a common target  $\tilde{\rho}_2$  grid with uniformly fine spacing of  $\Delta\tilde{\rho}_2 = 0.1 \text{ kg/m}^3$ . Because the **rho2** diagnostics are already binned in  $\tilde{\rho}_2$  coordinates online, the WMT budgets for **rho2** are independent of the averaging interval; however, the relatively coarse bins of the  $\tilde{\rho}_2$  grid used for the online diagnostics (see bin limits in Figure 10) obscures interesting finer-scale features of the  $\rho_2$ -WMT budget (compare panels g and h to i).

616 Next, we repeat our calculation of the  $\rho_2$ -WMT budget but now use a target  $\tilde{\rho}_2$   
 617 grid that differs significantly from the online diagnostic grid (Figure 11), in particular  
 618 by making the  $\tilde{\rho}_2$  bin spacing much finer at lower densities. As before, the calculations  
 619 employing monthly-mean depth-level and hybrid coordinate diagnostics are fairly noisy  
 620 but converge reasonably well when dropped to daily-means. Again, the  $\rho_2$  calculations  
 621 remain by construction independent of the averaging interval; however, comparison with  
 622 the brute-forced calculations using hourly-mean diagnostics in depth-level and prognostic  
 623 hybrid coordinates (Figure 11g-i) reveals that the online-binning in  $\tilde{\rho}_2$  coordinates

624 obscures interesting leading-order features at scales finer than the diagnostic  $\tilde{\rho}_2$  grid, and  
 625 which can not be recovered.

626 Finally, we repeat the same exercise but for a  $\Theta$ -WMT budget. Because Conser-  
 627 vative Temperature  $\Theta$  was not yet available as an online diagnostic coordinate in MOM6,  
 628 all three sets of diagnostics were transformed into  $\Theta$  coordinates offline. From the top  
 629 row of Figure 12, we observe that offline calculations with monthly-mean diagnostics are  
 630 noisy, while those with daily-mean diagnostics are quite similar to the hourly-mean/timestep  
 631 ones. Interestingly, the density-coordinate calculations differ substantially from those with  
 632 the depth-level and prognostic hybrid coordinates, which are themselves in agreement.  
 633 These errors appear to be due to the very low effective resolution of the density-coordinate  
 634 grid in the shallow and fresh inner Baltic Sea (see Figures 3 and 11), meaning the whole  
 635 water column is in some cases represented by a single density layer, over which the  $\Theta$   
 636 values and  $\Theta$ -tendency diagnostics are then averaged.

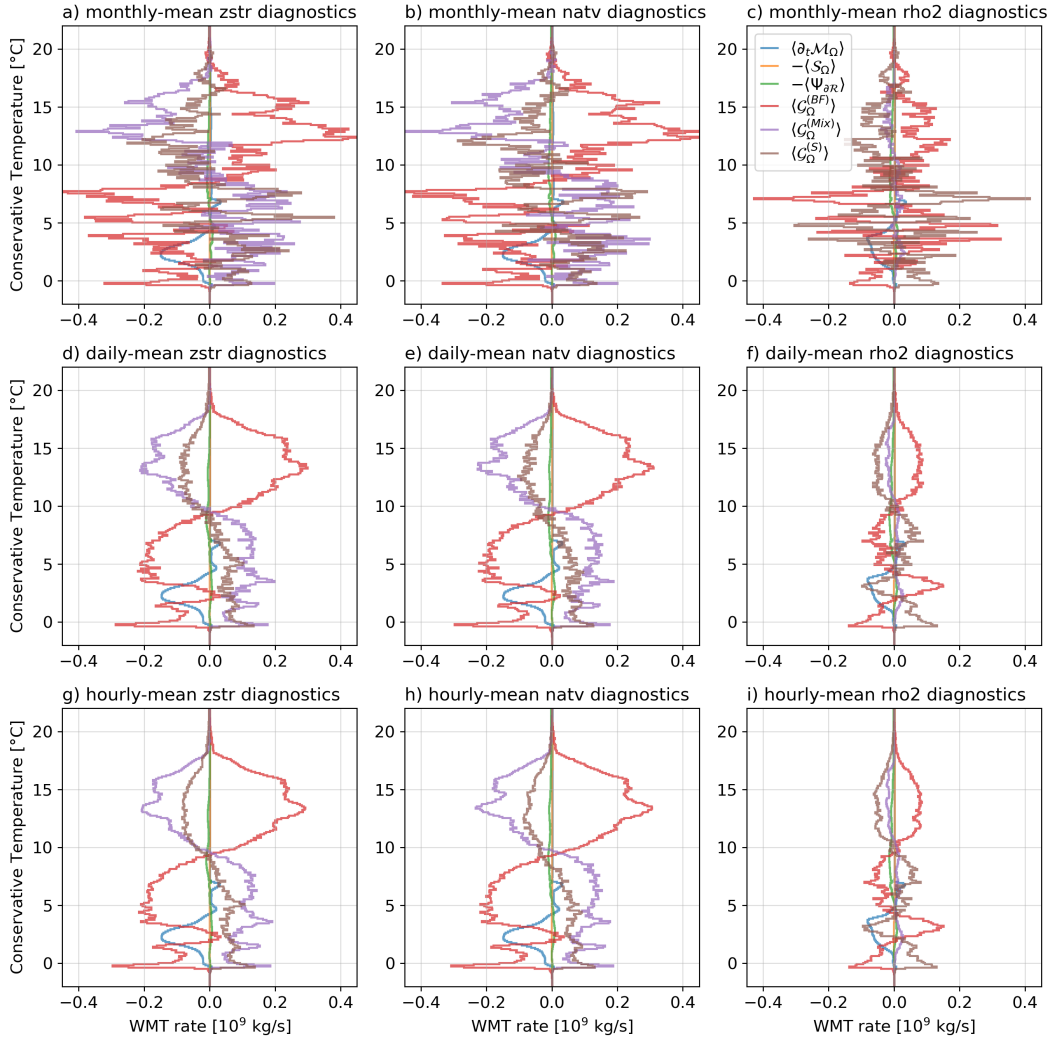


**Figure 12.** Sensitivity of annual-mean  $\Theta$ -WMT budgets to the diagnostic averaging interval  $\Delta t$  (rows) and the diagnostic vertical coordinate (columns), where **zstr** denotes depth-levels, **natv** denotes prognostic hybrid coordinate levels, and **rho2** denotes potential density surfaces referenced to 2000 dbar. The **rho2** diagnostics do not converge to the correct values because most of the Baltic Sea occupies the single lightest layer of the diagnostic potential density grid.

637 For most ocean model applications, outputting thousands of three-dimensional ten-  
 638 dency fields with an averaging interval shorter than the inherent variability of the model  
 639 is resource-intensive and largely untenable. Instead, it is recommended that all required  
 640 diagnostics be conservatively regridded and remapped online into  $\tilde{\lambda}$  coordinate bins af-  
 641 ter each tracer timestep, so that longer-term time-averaged diagnostics can be meaning-  
 642 fully accumulated (at the cost of slower model run times) and more readily analyzed. Such  
 643 online remapping of diagnostics was recommended as part of the OMIP exercise by Griffies  
 644 et al. (2016), with this technology becoming more standard across ocean climate model  
 645 codes. However, the leading-order differences between the various  $\lambda$ -WMT budgets de-  
 646 scribed above (Figures 10-12) serve as a caution that one should carefully tune their di-  
 647 agnostic coordinates to the problem at hand to avoid the risk of ending up with noisy  
 648 or misleading WMT budgets. (In the case of the Baltic Sea simulation described here,  
 649 the employed diagnostic  $\tilde{\rho}_2$  grid was previously calibrated to capture features of the Merid-  
 650 ional Overturning Circulation in global climate model configurations, so it is not surpris-  
 651 ing that it poorly resolves water masses in the marginal Baltic Sea.)

## 652 4 Outlook

653 As Water Mass Transformation (WMT) analysis becomes an increasingly popu-  
 654 lar tool for advancing understanding of ocean circulation (Tesdal et al., 2023; Evans et  
 655 al., 2023) and coupled climate dynamics (Deppenmeier et al., 2022), it is all the more  
 656 important that the methods used to diagnose terms in WMT budgets be correct and that  
 657 the scientific interpretations of these results be robust. We intend for this self-contained  
 658 presentation of the theory and practice of diagnosing WMT budgets to be a useful refer-  
 659 ence for practitioners of water mass analysis, especially (but not only) as applied to  
 660 numerical ocean models. We contend that full WMT budgets are an under-utilized tool  
 661 in the ocean and climate modeler’s toolbox, with applications to both model develop-  
 662 ment (e.g., identifying the processes causing water mass biases, circulation biases, and  
 663 unwanted spurious mixing and control model drift) and scientific discovery (e.g., attribut-  
 664 ing the drivers of variability and change in water mass properties and overturning cir-  
 665 culations).

666 The method for diagnosing  $\lambda$ -WMT budgets presented here requires the scalar field  
 667  $\lambda$  to satisfy a conservation equation of the form (16) and that the diagnostics for each  
 668 of the terms in the conservation budget be available, as described in Appendix A. This  
 669 is generally true for prognostic tracers, i.e. tracers that are time-stepped within a FV-  
 670 GVC ocean model, such as temperature, salinity, and biogeochemical tracers. Diagnos-  
 671 tic tracers, which are instead derived from the prognostic tracers using algebraic equa-  
 672 tions or elliptic partial differential equations, however, do not necessarily satisfy exact  
 673 conservation equations of the form required for water mass transformation analysis.

674 Seawater *in-situ* density,  $\rho$ , is an example of a more complicated diagnostic tracer,  
 675 as it depends nonlinearly on temperature, salinity, and pressure (T. McDougall et al.,  
 676 2009). Because gravity acts upon seawater density gradients, it would be advantageous  
 677 to analyze oceanic flows along surfaces over which this buoyancy force vanishes, i.e., *neu-*  
 678 *tral surfaces*, and to diagnose diapycnal transformations across them. Unfortunately,  
 679 however, the locally referenced (*in-situ*) seawater density can vary substantially under  
 680 purely adiabatic displacements (i.e.  $\delta\Theta = \delta S = 0$  but  $\delta p \neq 0$ ), making it an inappro-  
 681 priate choice for a dynamically-useful density coordinate. These compressibility effects  
 682 can be accounted for by instead considering the *potential density*,

$$\rho_r(\Theta, S) \equiv \rho(\Theta, S, r), \quad (43)$$

683 defined as the hypothetical density sea water would have if brought adiabatically to a  
 684 constant reference pressure,  $p = r$ . Following Groeskamp et al. (2019), changes in po-  
 685 tential density,  $\rho_r$ , can then be usefully expressed just in terms of changes in Conserva-

686 tive Temperature,  $\Theta$ , and Absolute Salinity,  $S$ ,

$$\delta\rho_r = \rho \left[ -\left(-\frac{1}{\rho} \frac{\partial\rho_r}{\partial\Theta}\right) \delta\Theta + \left(\frac{1}{\rho} \frac{\partial\rho_r}{\partial S}\right) \delta S \right], \quad (44)$$

687 where  $\alpha_r \equiv -\frac{1}{\rho} \frac{\partial\rho_r}{\partial\Theta}$  and  $\beta_r \equiv \frac{1}{\rho} \frac{\partial\rho_r}{\partial S}$  are both referenced to  $p = r$ . Dia- $\rho_r$  transforma-  
688 tions are thus simply diagnosed as

$$\frac{D\rho_r}{Dt} = \rho \left( -\alpha_r \frac{D\Theta}{Dt} + \beta_r \frac{DS}{Dt} \right), \quad (45)$$

689 where  $\alpha_r = \alpha_r(\mathbf{x}, t; r)$  is the (usually positive) thermal expansion coefficient,  $\beta_r = \beta_r(\mathbf{x}, t; r) >$   
690  $0$  is the positive haline contraction coefficient, and  $\frac{D}{Dt} \equiv \lim_{\delta t \rightarrow 0} \frac{\delta}{\delta t}$  is the material deriva-  
691 tive. The density-coordinate calculations presented here take  $r = 2000$  dbar because  
692 budget diagnostics remapped online to the corresponding potential density  $\rho_2$  were read-  
693 ily available.

694 While the global self-consistency of potential density surfaces is a useful charac-  
695 teristic for water mass analysis, it nevertheless suffers from two important interpreta-  
696 tive limitations: 1) it is *in-situ* density, not potential density, that appears in the mo-  
697 mentum equation and 2) away from the reference pressure, adiabatic displacements along  
698 potential density surfaces generally cause buoyant restoring forces, and thus dia-neutral  
699 transformation! In a potential density framework, we are therefore unable to isolate the  
700 desired dianeutral contributions to dia- $\rho_r$  transformations from potentially non-negligible  
701 isoneutral contributions. This limitation is likely exacerbated for studies of deep ocean  
702 overturning, for which we would like to compare surface-forced water mass transforma-  
703 tions (at  $p = p_{\text{atm}}$ ) against abyssal mixing-driven transformations (at  $p > 4000$  dbar).

704 For global-scale water mass analysis, it would thus be desirable to define a *neutral*  
705 *density* variable that satisfies the following three desirable properties: 1) its isosurfaces  
706 are neutral surfaces, 2) it is quasi-material, i.e., changes only due to material transfor-  
707 mations of temperature and salinity, and 3) is pycnotropic, i.e., can be expressed as a  
708 function of only *in-situ* density and pressure. While it turns out to be impossible to de-  
709 fine exactly neutral surfaces for the global ocean, Stanley et al. (2021) demonstrate that  
710 it is possible to construct *approximately neutral surfaces* that satisfy property 1, and hence  
711 also properties 2 and 3, to a reasonable degree—or at least better than existing alterna-  
712 tives, such as the commonly-used “neutral density” variable proposed by Jackett and Mc-  
713 Dougall (1997) and later applied to WMT analysis by Iudicone et al. (2008). Future work  
714 includes extending our water mass transformation methods to density variables that are  
715 more neutral than potential density referenced to 2000 dbar,  $\rho_2$ .

716 In describing the conventional methods of water mass transformation analysis in  
717 detail, we have omitted a broader discussion of recent developments in water mass anal-  
718 ysis that provide complementary perspectives: circulation and transformation in tracer-  
719 tracer coordinates (Zika et al., 2012; ?, ?; Evans et al., 2018), constant-mass partition-  
720 ing (Sohail et al., 2023), Lagrangian water mass transformations (Döös et al., 2008; Tam-  
721 sitt et al., 2018), internal tracer content (Holmes et al., 2019; Bladwell et al., 2021), wa-  
722 ter mass-based inverse methods (Zika & Taimoor, 2023), and applications to biogeochem-  
723 istry (Iudicone et al., 2011). Practitioners of water mass analysis should choose whichever  
724 method (or combination of methods) best suits the problem at hand.

725 Budget diagnostics suitable for full WMT budget analysis are typically not avail-  
726 able from commonly used repositories of ocean and climate model data, such as the CMIP  
727 ESGF data portals. For temperature, salinity, and density, surface water mass transfor-  
728 mations and lateral convergent transports can be computed using monthly-mean sur-  
729 face flux and horizontal mass transport diagnostics, respectively, both of which are des-  
730 ignated as Priority 1 in the OMIP protocol (Griffies et al., 2016). Full mass and tracer  
731 budget diagnostics, which include the interior mixing tendencies, are only asked to be

732 saved at annual-mean resolution at Priority 3. The FAFMIP protocol elevates these annual-  
 733 means to Priority 1 and asks for monthly-means at Priority 2; the monthly-mean diag-  
 734 nostics are useful for resolving the seasonal cycle of these budgets in geographical-depth  
 735 space, but can result in substantial errors when transformed offline into tracer coordi-  
 736 nates (compare rows of Figure 12). To our knowledge, snapshots of layer-thickness and  
 737 tracer concentration/content, which are required at the bounds of the budget time-averaging  
 738 intervals to accurately close the WMT budget, are not included in the OMIP, FAFMIP,  
 739 or any other MIP protocol; however, it may be possible to approximate these tenden-  
 740 cies sufficiently well for some use cases by finite-differencing monthly-mean layer thick-  
 741 ness diagnostics and interpolating the results to the middle of the months. As demon-  
 742 strated here, accurate WMT budgets require closed mass and tracer budgets that are  
 743 either output at sufficiently high frequency—more often than monthly for global climate  
 744 simulations—or are regridded and remapped online into the target tracer coordinate (see  
 745 Figure 10). In either case, the raw data can be prohibitively large due to their four-dimensional  
 746 nature and the large number of variables required to close the WMT budgets, which is  
 747 presumably one reason these diagnostics are not already more available. At GFDL, this  
 748 data proliferation problem has been mitigated in the development and production of mesoscale  
 749 eddy-rich simulations by remapping to target tracer coordinates online and conservatively  
 750 coarsening the diagnostics in time (as monthly- or annual-means) and in the horizon-  
 751 tal dimensions (by integrating over 2x2 grid cell tiles). We argue that intercomparison  
 752 of modeled WMT budgets would be sufficiently helpful for model development, evalu-  
 753 ation, and analysis to warrant the inclusion of suitable ocean model diagnostics in fu-  
 754 ture MIP protocols. We call on the community to initiate proof-of-concept inter-model  
 755 comparisons in support of a Water Mass Model Intercomparison Project (WMMIP).

756 Provided that model data suitable for full WMT budgets becomes available, ro-  
 757 bust model intercomparison will require the standardization of analysis methods. As we  
 758 have demonstrated here, there are several subtleties involved in the diagnosis of WMT  
 759 budgets through which differences in implementation could introduce spurious inter-model  
 760 differences. We developed the `xwmb` stack of Python packages (see Appendix D) as a model-  
 761 agnostic community tool to standardize the diagnosis of WMT budgets in models and  
 762 to facilitate robust model intercomparisons. For each distinct ocean model, the package  
 763 only requires the specification of the model’s grid geometry (using `xgcm`) and the struc-  
 764 ture of its mass and tracer budgets (using `xbudget`). Future work will extend support  
 765 to arbitrary grid topologies such as the cubed-sphere grid of ECCOv4 (Forget et al., 2015)  
 766 or the unstructured mesh of MPAS-Ocean (Ringler et al., 2013).

767 In conclusion, the development of increasingly comprehensive and high-resolution  
 768 numerical ocean models requires new diagnostics that can extract meaning from the chaos;  
 769 water mass transformation theory provides a framework for integrating these big and com-  
 770 plex data sets to produce physically interpretable scalar budgets. The advances outlined  
 771 here provide a set of best practices and software tools for robust calculations and inter-  
 772 pretations of water mass transformation budgets—we encourage you to use them!

## 773 **Appendix A Diagnosis of water mass transformation rates**

### 774 **A1 Relationship between advective- and flux-forms of the material deriva-** 775 **tive**

776 Budget diagnostics for finite-volume ocean models are often not immediately avail-  
 777 able in the *intensive* form (16),  $\rho \frac{D\lambda}{Dt} = \rho \dot{\lambda}$ , or

$$\rho \frac{D\lambda}{Dt} \equiv \rho \left( \frac{\partial \lambda}{\partial t} + \mathbf{v} \cdot \nabla \lambda \right) = -\nabla \cdot \mathbf{J}, \quad (\text{A1})$$

778 which exposes the advective-form material derivative that is necessary for the WMT bud-  
 779 get approach outlined in Section 2. To write equation (A1), we have assumed all of the

780 material transformation processes represented in  $\rho \dot{\lambda}$  can be expressed as the convergence  
 781 of a density-weighted tracer flux<sup>1</sup>  $\mathbf{J}$ , which we take to include fluxes across the ocean  
 782 boundary (or, equivalently, the oceanic fluxes they induce infinitesimally close by).

783 Many ocean models employ discretizations that fall under the class of Generalized  
 784 Vertical Coordinate (GVC) models (Chassignet et al., 2006), in which the GVC, denoted  
 785  $\sigma$ , is discretized in a number  $N$  of  $k$ -indexed layers of thickness  $h_k \equiv \int_{\sigma_{k-1/2}}^{\sigma_{k+1/2}} z_\sigma d\sigma$ . The  
 786 function  $z(\sigma)$  must be a strictly monotonic mapping such that the specific thickness  $z_\sigma \equiv$   
 787  $\frac{\partial z}{\partial \sigma}$  (in  $\sigma$ -coordinates) is single-signed. In such models, tracer budgets are diagnosed in  
 788 the *extensive* (layer-integrated) form (Griffies et al. (2020), eq. 32)

$$\frac{\partial(h_k \overline{\rho \lambda^k})}{\partial t} + \nabla_\sigma \cdot (h_k \overline{\rho \lambda \mathbf{u}^k} + h_k \overline{\mathbf{J}^k}) + \Delta_\sigma^k (\rho \lambda w^{(\dot{\sigma})} + J^{(\sigma)}) = 0 \quad (\text{A2})$$

789 which also corresponds with the models' prognostic conservation equations. In equation  
 790 (A2), overbars ( $\overline{\phi^k} = \frac{1}{h_k} \int_{\sigma_{k-1/2}}^{\sigma_{k+1/2}} \phi z_\sigma d\sigma$ ) denote the layer-average operation;  $J^{(\sigma)} =$   
 791  $z_\sigma \nabla \sigma \cdot \mathbf{J}$  is the thickness-weighted dia- $\sigma$  flux;  $\nabla_\sigma$  is the along- $\sigma$  gradient;  $\Delta_\sigma^k \phi = \phi(\sigma_{k+1/2}) -$   
 792  $\phi(\sigma_{k-1/2})$  is the finite difference across the  $k^{\text{th}}$  layer; and  $\rho$ ,  $\lambda$ , and  $\mathbf{u}$  are the density,  
 793 tracer concentration, and horizontal velocity, respectively. The dia- $\sigma$  velocity component  
 794 for the GVC is denoted by  $w^{(\dot{\sigma})} \equiv z_\sigma \frac{D\sigma}{Dt} \equiv z_\sigma \dot{\sigma}$ , which is a normalization of the dia- $\sigma$   
 795 advective mass flux in terms of a horizontal area element  $dA$ , defined by  $\rho w^{(\dot{\sigma})} dA \equiv$   
 796  $\rho (\mathbf{v} - \mathbf{v}^{(\sigma)}) \cdot \hat{\mathbf{n}} dS$  (Griffies et al. (2020), Appendix D).

797 To recover the evolution equation (A1) for the intensive tracer concentration  $\lambda$ , we  
 798 must remove from the extensive layer-integrated budget (A2) the effects of an evolving  
 799 layer mass per unit area  $\bar{h}\rho$ , given by (Griffies et al. (2020), eq. 32b)

$$\frac{\partial(h_k \bar{\rho}^k)}{\partial t} + \nabla_\sigma \cdot (h_k \overline{\rho \mathbf{v}^k}) + \Delta_\sigma^k (\rho \lambda w^{(\dot{\sigma})}) = 0. \quad (\text{A3})$$

800 Since information has already been irreversibly lost by integration between the con-  
 801 tinuous form (A1) and the vertically discrete layer-integrated form (A2), however, we  
 802 take a step back and consider the continuous versions of the thickness-weighted budgets  
 803 (Griffies (2024), 58.4):

$$\frac{\partial(\rho z_\sigma \lambda)}{\partial t} + \nabla_\sigma \cdot (\rho z_\sigma \lambda \mathbf{v}) + \frac{\partial}{\partial \sigma} (\rho z_\sigma \lambda \dot{\sigma}) = - \left[ \nabla_\sigma \cdot (z_\sigma \mathbf{J}) + \frac{\partial}{\partial \sigma} (z_\sigma \nabla \sigma \cdot \mathbf{J}) \right], \quad (\text{A4})$$

$$\frac{\partial(\rho z_\sigma)}{\partial t} + \nabla_\sigma \cdot (\rho z_\sigma \mathbf{v}) + \frac{\partial}{\partial \sigma} (\rho z_\sigma \dot{\sigma}) = 0. \quad (\text{A5})$$

804 Note that under the Boussinesq approximation ( $\nabla \cdot \mathbf{v} = 0$ ) and with geopotential co-  
 805 ordinates ( $\sigma = z$ ), the specific cell thickness  $z_\sigma = 1$  and reference density  $\rho = \rho_0$  are  
 806 constant and can be pulled out of the derivatives such that (A4) reduces trivially to (A1).

807 In the non-Boussinesq GVC case, expanding each of the LHS terms of (A4) using  
 808 the product rule, we can write the respective terms in equation (A1) as:

$$\rho \frac{\partial \lambda}{\partial t} = \frac{1}{z_\sigma} \left[ \frac{\partial(\rho z_\sigma \lambda)}{\partial t} - \lambda \frac{\partial(\rho z_\sigma)}{\partial t} \right] \quad (\text{A6})$$

$$\rho \mathbf{v} \cdot \nabla \lambda \equiv \rho \left( \mathbf{v} \cdot \nabla_\sigma \lambda + \dot{\sigma} \frac{\partial \lambda}{\partial \sigma} \right) = \frac{1}{z_\sigma} \left[ \nabla_\sigma \cdot (\rho z_\sigma \lambda \mathbf{v}) - \lambda \nabla_\sigma \cdot (\rho z_\sigma \mathbf{v}) + \frac{\partial}{\partial \sigma} (\rho z_\sigma \lambda \dot{\sigma}) - \lambda \frac{\partial}{\partial \sigma} (\rho z_\sigma \dot{\sigma}) \right] \quad (\text{A7})$$

$$\rho \dot{\lambda} = \frac{-1}{z_\sigma} \left[ \nabla_\sigma \cdot (z_\sigma \mathbf{J}) + \frac{\partial}{\partial \sigma} (z_\sigma \nabla \sigma \cdot \mathbf{J}) \right], \quad (\text{A8})$$

<sup>1</sup> It is straight-forward to extend the method to include non-flux-form tracer sources and sinks; we leave these out to simplify the exposition as much as possible.

809 where each of the terms now corresponds directly with the continuous versions of the ex-  
 810 tensive tracer and mass budget diagnostics. To further connect these to finite-volume  
 811 diagnostics, we now integrate (A6-A8) over discrete  $\sigma$ -layers, but first multiplying both  
 812 sides by  $z_\sigma$  because the intensive  $\lambda$ -budgets only appear as thickness-weighted integrands,  
 813 e.g.  $\rho \frac{\partial \lambda}{\partial t} dV$ , where  $dV = dz dA = z_\sigma d\sigma dA$ .

814 For the tendency term, the  $\sigma$ -integral commutes with time derivatives and we have

$$h_k \rho \overline{\frac{\partial \lambda}{\partial t}} \equiv \int_{\sigma_{k-1/2}}^{\sigma_{k+1/2}} \rho z_\sigma \frac{\partial \lambda}{\partial t} d\sigma = \left[ \frac{\partial}{\partial t} \right]_\sigma (h_k \overline{\rho \lambda^k}) - \int_{\sigma_{k-1/2}}^{\sigma_{k+1/2}} \lambda \frac{\partial(\rho z_\sigma)}{\partial t} d\sigma = \left[ \frac{\partial}{\partial t} \right]_\sigma (h_k \overline{\rho \lambda})^k - \bar{\lambda}_k \left[ \frac{\partial}{\partial t} \right]_\sigma (h_k \bar{\rho}^k), \quad (\text{A9})$$

815 where we have ignored intra-layer spatial correlations between  $\lambda$  and  $\frac{\partial(\rho z_\sigma)}{\partial t}$ .

816 For the advection term, derivatives also commute and we similarly arrive at

$$h_k \overline{\rho \mathbf{v} \cdot \nabla \lambda^k} = \nabla_\sigma \cdot (h_k \overline{\rho \lambda \mathbf{v}^k}) + \Delta_\sigma^k (\rho w^{(\dot{\sigma})} \lambda) - \bar{\lambda}^k \left[ \nabla_\sigma \cdot (h_k \overline{\rho \mathbf{v}^k}) + \Delta_\sigma^k (\rho w^{(\dot{\sigma})}) \right]. \quad (\text{A10})$$

817 For the non-conservative processes, we have

$$h_k \overline{\rho \dot{\lambda}^k} = - \left[ \nabla_\sigma \cdot (h_k \overline{\mathbf{J}^k}) + \Delta_\sigma^k J^{(\sigma)} \right]. \quad (\text{A11})$$

818 Altogether, we have the following finite-volume expressions for the layer-mass-weighted  
 819  $\lambda$ -conservation equation

$$\left[ \frac{\partial}{\partial t} (h_k \overline{\rho \lambda^k}) - \bar{\lambda}^k \frac{\partial}{\partial t} (\bar{\rho}^k h_k) \right] \quad h_k \overline{\rho \frac{\partial \lambda^k}{\partial t}} \quad (\text{A12})$$

$$+ \left[ \nabla_\sigma \cdot (h_k \overline{\rho \lambda \mathbf{v}^k}) + \Delta_\sigma^k (\rho w^{(\dot{\sigma})} \lambda) - \bar{\lambda}^k \left( \nabla_\sigma \cdot (h_k \overline{\rho \mathbf{v}^k}) + \Delta_\sigma^k (\rho w^{(\dot{\sigma})}) \right) \right] \Leftrightarrow + h_k \overline{\rho \mathbf{v} \cdot \nabla \lambda^k} \quad (\text{A13})$$

$$= - \left[ \nabla_\sigma \cdot (h_k \overline{\mathbf{J}^k}) + \Delta_\sigma^k J^{(\sigma)} \right] \quad = h_k \overline{\rho \dot{\lambda}^k} \quad (\text{A14})$$

## 820 A2 Kinematics of normal-flux boundary conditions

821 We now turn to a discussion of the subtleties related to the treatment of kinematic  
 822 boundary conditions on fluxes of seawater mass and tracer content. We will consider both  
 823 advective exchange fluxes that reflect the exchange of mass between the ocean and other  
 824 Earth system components (e.g. precipitation, evaporation, sea ice melt), as well as non-  
 825 advective tracer exchange fluxes (e.g. turbulent air-sea fluxes, radiative heating/cooling,  
 826 sea ice brine rejection).

827 We label the  $N+1$  layer interfaces with integers ( $k = 0, 1, \dots, N$ ) and the  $N$  layer  
 828 centers or layer averages with the half-steps between them ( $k = \frac{1}{2}, \dots, N - \frac{1}{2}$ ). This in-  
 829 dex notation is shifted by  $\frac{1}{2}$  relative to that used by others (e.g. Griffies et al. (2020));  
 830 however, it greatly simplifies the interpretation of the following derivation. We take  $k =$   
 831  $0$  to be the sea surface and  $k = N$  the sea floor. Then, to explicitly reveal the influ-  
 832 ence of boundary conditions, we consider the three flux categories (bottom-interfacing,

833 interior, surface-interfacing) separately<sup>2</sup>:

$$\text{(density-weighted tracer)} \qquad \qquad \qquad \text{(mass)} \qquad \qquad \qquad \text{(A15)}$$

$$\Delta_{\sigma}^k(\rho w^{(\dot{\sigma})}\lambda + J^{(\sigma)}) \qquad \qquad \qquad \Delta_{\sigma}^k(\rho w^{(\dot{\sigma})}) \qquad \qquad \qquad \text{(A16)}$$

$$= \Delta_{\sigma}^k \left( \mathcal{H}(k-N) \left[ \rho w^{(\dot{\sigma})}\lambda + J^{(\sigma)} \right] \right) \qquad = \qquad \Delta_{\sigma}^k \left( \mathcal{H}(k-N) \left[ \rho w^{(\dot{\sigma})} \right] \right) \quad \text{(bottom ocean fluxes)} \qquad \text{(A17)}$$

$$+ \Delta_{\sigma}^k \left( \mathcal{I}_0^N(k) \left[ \rho w^{(\dot{\sigma})}\lambda + J^{(\sigma)} \right] \right) \qquad + \qquad \Delta_{\sigma}^k \left( \mathcal{I}_0^N(k) \left[ \rho w^{(\dot{\sigma})} \right] \right) \quad \text{(interior ocean fluxes)} \qquad \text{(A18)}$$

$$+ \Delta_{\sigma}^k \left( \mathcal{H}(-k) \left[ \rho w^{(\dot{\sigma})}\lambda + J^{(\sigma)} \right] \right), \qquad + \qquad \Delta_{\sigma}^k \left( \mathcal{H}(-k) \left[ \rho w^{(\dot{\sigma})} \right] \right) \quad \text{, (surface ocean fluxes)} \qquad \text{(A19)}$$

834 where  $\mathcal{H}(n)$  is the Heaviside function (1 if  $n \geq 0$ ; 0 otherwise) and  $\mathcal{I}_i^j(k)$  is the interior  
 835 function<sup>3</sup> (1 if  $0 < k < N$ ; 0 otherwise). To illustrate the utility of the Heaviside  
 836 function notation, consider the expressions for the ocean bottom fluxes (A17), which only  
 837 have a nonzero contribution within the bottom-interfacing layer ( $k = N-1/2$ ), where  
 838  $\Delta_{\sigma}^k(\mathcal{H}(k-N)\phi) = \mathcal{H}(0)[\phi]_{k=N} - \mathcal{H}(-1)[\phi]_{k=N-1} = [\phi]_{k=N}$  is just the dia-seafloor  
 839 flux, as desired. Since interior fluxes are typically already diagnosed in the form of ex-  
 840 pression (A18), where  $\mathcal{I}_0^N(k)J^{(\sigma)}$  represent interior diffusive fluxes, we do not need to  
 841 manipulate them any further. The surface and bottom oceanic fluxes, on the other hand,  
 842 are provided only in terms of the interfacial advective and non-advective exchange fluxes  
 843 that induce them.

844 At the bottom, the advective mass and tracer fluxes both vanish due to the no-normal  
 845 flow boundary condition on the barycentric velocity ( $\mathbf{v} \cdot \hat{\mathbf{n}} = 0$ ) at the static bound-  
 846 ary ( $\mathbf{v}^{(b)} = 0$ ), which together yield  $\rho(\mathbf{v} - \mathbf{v}^{(b)}) \cdot \hat{\mathbf{n}} dS = 0$  and thus  $\rho w^{(\dot{\sigma})} = 0$ . How-  
 847 ever, there may still be a nonzero non-advective tracer transport (e.g. geothermal heat  
 848 flux), which we denote as  $J^{(\sigma)} \equiv -Q_{\lambda}^{\text{bot}}$  such that  $Q_{\lambda}^{\text{bot}} > 0$  indicates an input of density-  
 849 weighted  $\lambda$  to the ocean. Thus, we write the bottom fluxes as

$$\left[ J^{(\sigma)} \right]_{k=N} = -Q_{\lambda}^{\text{bot}} \qquad \qquad \qquad \text{(A20)}$$

$$\left[ \rho w^{(\dot{\sigma})} \right]_{k=N} = 0 \qquad \qquad \qquad \text{(A21)}$$

850 At the sea surface, the mass flux  $Q_M^{\text{surf}}$  (e.g. due to precipitation, evaporation, sea  
 851 ice melt) is, by definition, purely advective, yielding the straight-forward equivalence

$$\left[ \rho w^{(\dot{\sigma})} \right]_{k=0} = -Q_M^{\text{surf}}. \qquad \qquad \qquad \text{(A22)}$$

852 By contrast, the net density-weighted tracer exchange flux  $Q_{\lambda}^{\text{net}}$  must be treated  
 853 carefully because it includes a non-advective component as well as an advective compo-  
 854 nent associated with the tracer content of the water being exchanged,

$$Q_{\lambda}^{\text{net}} = \lambda_M Q_M^{\text{surf}} + Q_{\lambda}^{\text{surf}}, \qquad \qquad \qquad \text{(A23)}$$

<sup>2</sup> In practice, this conceptual approach is complicated by the fact that some boundary fluxes (most notably incoming solar radiation) penetrate across the interfaces and into the interior ocean, resulting in a non-negligible interior flux-divergence (Iudicone et al., 2008). It is nevertheless useful to distinguish the boundary-related processes from interior processes such as diffusion.

<sup>3</sup> The interior function differs from conventional boxcar functions because it excludes the endpoints.

855 where  $\lambda_M$  is the tracer concentration of the exchanged water mass<sup>4</sup>. Within an infinites-  
 856 imal skin layer of the surface ocean, this boundary exchange flux induces both an ad-  
 857 vective oceanic flux and a non-advective oceanic flux:

$$Q_\lambda^{\text{net}} = - \left[ \rho w^{\dot{\sigma}} \lambda + J^{(\sigma)} \right]_{k=0} = [\lambda]_{k=0} Q_M^{\text{surf}} - \left[ J^{(\sigma)} \right]_{k=0}. \quad (\text{A24})$$

858 Equating the RHS expressions of (A23) and (A24) yields an expression for the induced  
 859 non-advective oceanic flux in terms of the non-advective tracer exchange flux and the  
 860 advective mass flux:

$$[J^\sigma]_{k=0} = -Q_\lambda^{\text{surf}} - (\lambda_M - [\lambda]_{k=0})Q_M^{\text{surf}}. \quad (\text{A25})$$

861 In summary, plugging the above expressions back into equation (A19), we have

$$\left[ J^{(\sigma)} \right]_{k=0} = -Q_\lambda^{\text{surf}} - (\lambda_M - [\lambda]_{k=0})Q_M^{\text{surf}} \quad (\text{A26})$$

$$\left[ \rho w^{(\dot{\sigma})} \right]_{k=0} = -Q_M^{\text{surf}} \quad (\text{A27})$$

$$\left[ \rho w^{(\dot{\sigma})} \lambda \right]_{k=0} = -[\lambda]_{k=0} Q_M^{\text{surf}} \quad (\text{A28})$$

862 Altogether, plugging expressions (A20, A21, A26, A28, A27) into (A17–A19) we  
 863 have

$$\left[ \frac{\partial}{\partial t} (h_k \overline{\rho \lambda^k}) - \overline{\lambda^k} \frac{\partial}{\partial t} (\overline{\rho^k} h_k) \right] \quad (\text{A29})$$

$$+ \left[ \nabla_\sigma \cdot (h_k \overline{\rho \lambda^k} \mathbf{v}^k) + \Delta_\sigma^k \left( \mathcal{I}_0^N(k) \rho w^{(\dot{\sigma})} \lambda - \mathcal{H}(-k) \lambda Q_M^{\text{surf}} \right) \right] \quad (\text{A30})$$

$$- \overline{\lambda^k} \left[ \nabla_\sigma \cdot (h \overline{\rho \mathbf{v}^k}) + \Delta_\sigma^k \left( \mathcal{I}_0^N(k) \rho w^{(\dot{\sigma})} - \mathcal{H}(-k) Q_M^{\text{surf}} \right) \right] \quad (\text{A31})$$

$$= - \left[ \nabla_\sigma \cdot (h_k \overline{\mathbf{J}^k}) + \Delta_\sigma^k \left( \mathcal{I}_0^N(k) J^{(\sigma)} - \mathcal{H}(-k) \left[ Q_\lambda^{\text{surf}} + (\lambda_M - \lambda) Q_M^{\text{surf}} \right] - \mathcal{H}(k - N) Q_\lambda^{\text{bot}} \right) \right]. \quad (\text{A32})$$

864 If the Eulerian time derivative and advective components of the material derivative do  
 865 not need to be distinguished, then the terms with the common factor  $\overline{\lambda^k}$  outside of the  
 866 derivative/difference operators can be collectively identified as the conservative equation  
 867 for layer-integrated mass (A3), which therefore vanishes. We are left with:

$$h_k \rho \overline{\left( \frac{\partial \lambda}{\partial t} + \mathbf{v} \cdot \nabla \lambda \right)^k} \quad (\text{A33})$$

$$= \left[ \frac{\partial}{\partial t} (h_k \overline{\rho \lambda^k}) + \nabla_\sigma \cdot (h_k \overline{\rho \lambda^k} \mathbf{v}^k) + \Delta_\sigma^k \left( \mathcal{I}_0^N(k) \rho w^{(\dot{\sigma})} \lambda \right) - \Delta_\sigma^k \left( \mathcal{H}(-k) \lambda Q_M^{\text{surf}} \right) \right] \quad (\text{A34})$$

$$= - \left[ \nabla_\sigma \cdot (h_k \overline{\mathbf{J}^k}) + \Delta_\sigma^k \left( \mathcal{I}_0^N(k) J^{(\sigma)} - \mathcal{H}(-k) \left[ Q_\lambda^{\text{surf}} + (\lambda_M - \lambda) Q_M^{\text{surf}} \right] - \mathcal{H}(-(N - k)) Q_\lambda^{\text{bot}} \right) \right]. \quad (\text{A35})$$

868 Expression (A33) is the density-weighted and layer-integrated advective form of the kine-  
 869 matic material derivative; expression (A34) is the *flux form of the kinematic material*  
 870 *derivative*; and expression (A35) is the *flux-form of the non-conservative process-based ma-*  
 871 *terial derivative*. Breaking the budget down into the contributions from different classes

<sup>4</sup>This term could in principle be represented as the aggregate of multiple different mass fluxes, each carrying different mean tracer concentrations. In practice, assumptions are often much simpler; in MOM6, for example, both the in- and out-flowing water masses are assumed to have the same Conservative Temperature as the surface layer ( $\Theta_M = \overline{\Theta}^{k=0}$ ) and to be pure freshwater ( $S_M = 0$ ).

872 of physical processes, we assign the following labels:

$$\frac{\partial}{\partial t} (h_k \overline{\rho \lambda^k}) \quad (\text{Eulerian layer tendency}) \quad (\text{A36})$$

$$+ \nabla_{\sigma} \cdot (h_k \overline{\rho \lambda \mathbf{v}^k}) \quad (\text{Along-surface lateral advection}) \quad (\text{A37})$$

$$+ \Delta_{\sigma}^k \left( \mathcal{I}_0^N(k) \rho w^{(\sigma)} \lambda \right) \quad (\text{Dia-interface advection, i.e. regridding/remapping}) \quad (\text{A38})$$

$$- \Delta_{\sigma}^k (\mathcal{H}(-k) \lambda Q_M^{\text{surf}}) = \quad (\text{Advective ocean tracer flux at surface}) \quad (\text{A39})$$

$$- \nabla_{\sigma} \cdot (h_k \overline{\mathbf{J}^k}) \quad (\text{Along-layer lateral diffusion}) \quad (\text{A40})$$

$$- \Delta_{\sigma}^k \left( \mathcal{I}_0^N(k) J^{(\sigma)} \right) \quad (\text{Dia-interface turbulent diffusion}) \quad (\text{A41})$$

$$+ \Delta_{\sigma}^k (\mathcal{H}(-k) [Q_{\lambda}^{\text{surf}} + (\lambda_M - \lambda) Q_M^{\text{surf}}]) \quad (\text{Non-advective ocean tracer flux at surface}) \quad (\text{A42})$$

$$+ \Delta_{\sigma}^k (\mathcal{H}(-(N - k)) Q_{\lambda}^{\text{bot}}). \quad (\text{Non-advective ocean tracer flux at bottom}) \quad (\text{A43})$$

873 This partitioning of the layer-integrated tracer budget is useful because it is consistent  
 874 with the kinematic-process partitioning of the  $\lambda$ -WMT equation (24), allowing the in-  
 875 tegrals appearing therein to be approximated by Riemann sums and computed by 1) ap-  
 876 propriately area-weighting the terms (A36-A43), 2) vertically-remapping them to  $\lambda$ -coordinates,  
 877 3) and summing them over the discrete water class  $\Delta\Omega(\lambda, t) \equiv \Omega(\lambda + \Delta\lambda/2, t) \setminus \Omega(\lambda -$   
 878  $\Delta\lambda/2, t)$ , where  $\setminus$  denotes the set difference, as described in Section 3.

## 879 Appendix B Water mass transformation rates from MOM6 diagnos- 880 tics

881 The terms identified in expressions (A36-A43) are nearly identical to those avail-  
 882 able as layer-integrated tracer-budget diagnostics in MOM6,

$$\frac{\partial}{\partial t} (h_k \overline{\rho \lambda^k}) = \quad (\text{Eulerian layer tendency}) \quad (\text{B1})$$

$$- \nabla_{\sigma} \cdot (h_k \overline{\rho \lambda \mathbf{v}^k}) \quad (\text{Along-layer advection}) \quad (\text{B2})$$

$$- \Delta_{\sigma}^k \left( \mathcal{I}_0^N(k) \rho w^{(\sigma)} \lambda \right) \quad (\text{Dia-interface advection, i.e. regridding/remapping}) \quad (\text{B3})$$

$$- \nabla_{\sigma} \cdot (h_k \overline{\mathbf{J}^k}) \quad (\text{Along-surface lateral diffusion}) \quad (\text{B4})$$

$$- \Delta_{\sigma}^k \left( \mathcal{I}_0^N(k) J^{(\sigma)} \right) \quad (\text{Dia-interface turbulent diffusion}) \quad (\text{B5})$$

$$+ \Delta_{\sigma}^k (\mathcal{H}(-k) [Q_{\lambda}^{\text{surf}} + \lambda_M Q_M^{\text{surf}}]) \quad (\text{Surface tracer flux}) \quad (\text{B6})$$

$$+ \Delta_{\sigma}^k (\mathcal{H}(-(N - k)) Q_{\lambda}^{\text{bot}}). \quad (\text{Non-advective bottom tracer flux}), \quad (\text{B7})$$

883 Terms B2 and B3 can be moved to the LHS by changing signs. The more problematic  
 884 discrepancy is that, in the presently available layer-integrated MOM6 diagnostics, all of  
 885 the surface ocean tracer flux terms are bundled together (expression B6) and thus are  
 886 not readily decomposed into their purely advective part (A39), which contributes to the  
 887 kinematic material derivative (LHS), and the non-advective part (A42), which contributes  
 888 to the process-based material derivative (RHS). This means that the layer-integrated bud-  
 889 get diagnostics, as currently implemented, are inconsistent with the water mass trans-  
 890 formation approach! In the Baltic sea test case presented here, the erroneous transfor-  
 891 mations due to the omitted advective ocean tracer flux divergence term  $\Delta_{\sigma}^k (\mathcal{H}(-k) \lambda Q_M^{\text{surf}})$   
 892 are, relative to other terms in the budget,  $\mathcal{O}(10^{-2})$  for temperature but  $\mathcal{O}(1)$  for salin-  
 893 ity (for which  $\lambda_M = 0$  by assumption for freshwater, whereas  $\lambda = \mathcal{O}(30)$  ppt) and there-  
 894 fore can not be neglected.

895 While neither the advective ocean tracer flux divergence  $\Delta_\sigma^k (\mathcal{H}(-k)\lambda Q_M^{\text{surf}})$  nor the  
 896 non-advective ocean tracer flux divergence  $\Delta_\sigma^k (\mathcal{H}(-k) [Q_\lambda^{\text{surf}} + (\lambda_M - \lambda)Q_M^{\text{surf}}])$  are di-  
 897 rectly available as layer-integrated budget tendencies, they can be nevertheless be esti-  
 898 mated offline from the product of  $[\lambda]^{k=0}$  (often set to the upper-most layer's concentra-  
 899 tion  $[\lambda]^{k=\frac{1}{2}}$ ) and  $Q_M^{\text{surf}}$ . However, this offline operation inevitably omits temporal cor-  
 900 relation terms below the diagnostic averaging period, thereby introducing errors into the  
 901 otherwise exact budget. We recommend this approach eventually be replaced by a new  
 902 online diagnostic for  $\lambda Q_M^{\text{surf}}$ , ideally as a three-dimensional layer-integrated budget ten-  
 903 dency. In any case, subtracting the advective ocean tracer flux term from both sides of  
 904 equation (B1-B7) and rearranging the layer-integrated budget into the kinematic part  
 905 (LHS) and non-conservative process-based part (RHS), we arrive at the desired equa-  
 906 tion (A36-A43).

## 907 Appendix C Boussinesq relationships

908 Under the Boussinesq approximation, the flow field is non-divergent ( $\nabla \cdot \mathbf{v} = 0$ ),  
 909 which one might expect to simplify the water mass (or volume) budget. For instance,  
 910 directly integrating the continuity equation  $\nabla \cdot \mathbf{v} = 0$  over  $\Omega(\tilde{\lambda}, t)$  and following a sim-  
 911 ilar logic as in the above section, we have

$$- \int_{\Omega} \nabla \cdot \mathbf{v} dV = - \oint_{\partial\Omega} \mathbf{v} \cdot \hat{\mathbf{n}}^{(\partial\Omega)} dS = - \int_{\partial\Omega_{\text{surf}}} \mathbf{v} \cdot \hat{\mathbf{n}}^{(s)} dS - \int_{\partial\mathcal{R}} \mathbf{u} \cdot \hat{\mathbf{n}}^{(\partial\mathcal{R})} dS - \partial\lambda \int_{\Omega} \mathbf{v} \cdot \nabla \lambda dV = 0. \quad (\text{C1})$$

912 Additionally, by applying Leibniz' integral rule (6) to the volume budget (i.e., set-  
 913 ting  $F = 1$  instead of  $F = \rho$ ), we have

$$\partial_t \mathcal{V}_\Omega \equiv \partial_t \int_{\Omega} dV = \oint_{\partial\Omega} \mathbf{v}^{(\partial\Omega)} \cdot \hat{\mathbf{n}} dS = \int_{\partial\Omega_{\text{surf}}} \mathbf{v}^{(s)} \cdot \hat{\mathbf{n}}^{(s)} dS - \partial_{\tilde{\lambda}} \int_{\Omega} \frac{\partial\lambda}{\partial t} dV. \quad (\text{C2})$$

914 Summing (C1) and (C2), and using equation (16), yields a  $\lambda$ -water volume budget

$$\partial_t \mathcal{V}_\Omega + \int_{\partial\Omega_{\text{surf}}} (\mathbf{v} - \mathbf{v}^{(s)}) \cdot \hat{\mathbf{n}}^{(s)} dS + \int_{\partial\mathcal{R}} \mathbf{u} \cdot \hat{\mathbf{n}}^{(\partial\mathcal{R})} dS = -\partial_{\tilde{\lambda}} \left[ \int_{\Omega} \dot{\lambda} dV \right], \quad (\text{C3})$$

915 which is, modulo a reference density  $\rho = \rho_0$ , identical to the  $\lambda$ -WMT budget (29).

916 In theory, the possibility of separately evaluating the two components (C1 and C2)  
 917 might provide more granular insight into the WMT budget. Because boundary mass fluxes  
 918  $Q_M^{\text{surf}}$  are implemented directly in terms of the relative velocity  $\mathbf{v} - \mathbf{v}^{(s)}$ , equations (C1)  
 919 and (C2) are intrinsically coupled and can not be separately evaluated. In many cases,  
 920 however, the surface mass flux only plays a minor role in the water volume budget, such  
 921 that the following approximate relationships can still be useful (see Bailey et al., 2023):

$$\partial_t \mathcal{V}_\Omega \simeq -\partial_{\tilde{\lambda}} \int_{\Omega} \frac{\partial\lambda}{\partial t} dV \quad (\text{C4})$$

$$\int_{\partial\mathcal{R} \cap \{\lambda \leq \tilde{\lambda}\}} \mathbf{u} \cdot \hat{\mathbf{n}}^{(\partial\mathcal{R})} dS = -\partial_{\tilde{\lambda}} \int_{\Omega} \mathbf{v} \cdot \nabla \lambda dV \quad (\text{C5})$$

922 The utility of these approximate relationships may carry over to the non-Boussinesq case,  
 923 even as they become even less exact.

## 924 Appendix D Open Research

925 The calculations described above make use of a stack of new open-source Python  
 926 packages, which leverage data structures and methods from `xarray` (Hoyer & Hamman,

927 2017) and `xgcm` (Abernathy et al., 2022) for out-of-memory operations on finite volume  
928 model grids.

929 [Proper archiving and referencing of the following packages will be deferred to a  
930 later stage of the publication process]. We use the new package `regionate` to define our  
931 discretized regions  $R$  on the model grid and an updated version of `sectionate` to ac-  
932 cumulate mass transports normal to the boundary  $\partial R$  (see also Section 3.2). Water mass  
933 properties and transformation rates are evaluated using an updated version of `xwmt` (Tesdal  
934 et al., 2023). The remaining terms in the water mass budget are computed with the new  
935 package `xwmb`. An additional package, `xbudget`, provides helper functions for wrangling  
936 complicated multi-level tracer budget diagnostics and is used to verify budget closure  
937 and decompose high-level terms into constituent processes. All of the packages are de-  
938 signed to be agnostic to the specific formulation of the FV-GVC ocean model to promote  
939 community uptake and facilitate inter-model comparisons, requiring only that users pro-  
940 vide metadata describing each model’s grid geometry/topology and diagnostic mass/tracer  
941 budgets. The current implementations only support curvilinear grid but future work aims  
942 to develop support for arbitrary grid-face topologies (e.g. cubed-sphere) and grid geome-  
943 tries (i.e. unstructured triangular or hexagonal horizontal grids).

#### 944 **Acknowledgments**

945 H.F.D. acknowledges support from the NOAA C&GC Fellowship (AWARD NO.) and  
946 UC Irvine’s School of Physical Sciences.

#### 947 **References**

- 948 Abernathy, R. P., Busecke, J. J. M., Smith, T. A., Deauna, J. D., Banihirwe,  
949 A., Nicholas, T., ... Thielen, J. (2022, November). *xgcm*. Zenodo. Re-  
950 trieved 2023-08-07, from <https://zenodo.org/record/7348619> doi:  
951 10.5281/zenodo.7348619
- 952 Adcroft, A., Anderson, W., Balaji, V., Blanton, C., Bushuk, M., Dufour, C. O., ...  
953 Zhang, R. (2019). The GFDL Global Ocean and Sea Ice Model OM4.0: Model  
954 Description and Simulation Features. *Journal of Advances in Modeling Earth*  
955 *Systems*, 11(10), 3167–3211. Retrieved 2020-12-06, from [https://agupubs](https://agupubs.onlinelibrary.wiley.com/doi/abs/10.1029/2019MS001726)  
956 [.onlinelibrary.wiley.com/doi/abs/10.1029/2019MS001726](https://agupubs.onlinelibrary.wiley.com/doi/abs/10.1029/2019MS001726) (eprint:  
957 <https://agupubs.onlinelibrary.wiley.com/doi/pdf/10.1029/2019MS001726>) doi:  
958 <https://doi.org/10.1029/2019MS001726>
- 959 Bailey, S. T., Jones, C. S., Abernathy, R. P., Gordon, A. L., & Yuan, X. (2023,  
960 April). Water mass transformation variability in the Weddell Sea in ocean  
961 reanalyses. *Ocean Science*, 19(2), 381–402. Retrieved 2023-07-21, from  
962 <https://os.copernicus.org/articles/19/381/2023/> (Publisher: Coperni-  
963 cus GmbH) doi: 10.5194/os-19-381-2023
- 964 Bladwell, C., Holmes, R. M., & Zika, J. D. (2021, July). Internal Salt Content:  
965 A Useful Framework for Understanding the Oceanic Branch of the Water  
966 Cycle. *Journal of Physical Oceanography*, 51(7), 2167–2179. Retrieved 2024-  
967 02-27, from [https://journals.ametsoc.org/view/journals/phoc/51/7/](https://journals.ametsoc.org/view/journals/phoc/51/7/JPO-D-20-0212.1.xml)  
968 [JPO-D-20-0212.1.xml](https://journals.ametsoc.org/view/journals/phoc/51/7/JPO-D-20-0212.1.xml) (Publisher: American Meteorological Society Section:  
969 Journal of Physical Oceanography) doi: 10.1175/JPO-D-20-0212.1
- 970 Broecker, W. S. (1982). *Tracers in the Sea* (Edition unstated ed.). Eldigio Pr.
- 971 Burchard, H., & Rennau, H. (2008). Comparative quantification of physically and  
972 numerically induced mixing in ocean models. *Ocean Modelling*, 20, 293–311.
- 973 Cessi, P. (2019). The Global Overturning Circulation. *Annual Review of Marine Sci-*  
974 *ence*, 11(1), 249–270. Retrieved 2022-01-08, from [https://doi.org/10.1146/](https://doi.org/10.1146/annurev-marine-010318-095241)  
975 [annurev-marine-010318-095241](https://doi.org/10.1146/annurev-marine-010318-095241) (eprint: [https://doi.org/10.1146/annurev-](https://doi.org/10.1146/annurev-marine-010318-095241)  
976 [annurev-marine-010318-095241](https://doi.org/10.1146/annurev-marine-010318-095241)) doi: 10.1146/annurev-marine-010318-095241
- 977 Chassignet, E., Hurlburt, H., Smedstad, O. M., Halliwell, G., Wallcraft, A., Metzger,

- 978 E. J., ... Srinivasan, A. (2006, March). Generalized Vertical Coordinates for  
 979 Eddy-Resolving Global and Coastal Ocean Forecasts. *Oceanography*, 19(1),  
 980 118–129. Retrieved 2024-02-29, from [https://tos.org/oceanography/  
 981 article/generalized-vertical-coordinates-for-eddy-resolving-global  
 982 -and-coastal-ocea](https://tos.org/oceanography/article/generalized-vertical-coordinates-for-eddy-resolving-global-and-coastal-ocea) doi: 10.5670/oceanog.2006.95
- 983 de Lavergne, C., Madec, G., Le Sommer, J., Nurser, A. J. G., & Naveira Garabato,  
 984 A. C. (2016, February). On the Consumption of Antarctic Bottom Water  
 985 in the Abyssal Ocean. *Journal of Physical Oceanography*, 46(2), 635–661.  
 986 Retrieved 2019-01-02, from [http://journals.ametsoc.org/doi/10.1175/  
 987 JPO-D-14-0201.1](http://journals.ametsoc.org/doi/10.1175/JPO-D-14-0201.1) doi: 10.1175/JPO-D-14-0201.1
- 988 Deppenmeier, A.-L., Bryan, F. O., Kessler, W. S., & Thompson, L. (2022, Octo-  
 989 ber). Diabatic Upwelling in the Tropical Pacific: Seasonal and Subseasonal  
 990 Variability. *Journal of Physical Oceanography*, 52(11), 2657–2668. Retrieved  
 991 2023-07-20, from [https://journals.ametsoc.org/view/journals/phoc/  
 992 52/11/JPO-D-21-0316.1.xml](https://journals.ametsoc.org/view/journals/phoc/52/11/JPO-D-21-0316.1.xml) (Publisher: American Meteorological Society  
 993 Section: Journal of Physical Oceanography) doi: 10.1175/JPO-D-21-0316.1
- 994 Döös, K., Nilsson, J., Nycander, J., Brodeau, L., & Ballarotta, M. (2012). The  
 995 World Ocean thermohaline circulation. *Journal of Physical Oceanography*, 42,  
 996 1445–1460. doi: 10.1175/JPO-D-11-0163.1
- 997 Drake, H. F., Ferrari, R., & Callies, J. (2020, August). Abyssal Circulation Driven  
 998 by Near-Boundary Mixing: Water Mass Transformations and Interior Strat-  
 999 ification. *Journal of Physical Oceanography*, 50(8), 2203–2226. Retrieved  
 1000 2020-11-29, from [https://journals.ametsoc.org/jpo/article/50/8/2203/  
 1001 348530/Abyssal-Circulation-Driven-by-Near-Boundary-Mixing](https://journals.ametsoc.org/jpo/article/50/8/2203/348530/Abyssal-Circulation-Driven-by-Near-Boundary-Mixing) (Pub-  
 1002 lisher: American Meteorological Society) doi: 10.1175/JPO-D-19-0313.1
- 1003 Drake, H. F., Ruan, X., & Ferrari, R. (2022, November). Diapycnal Displace-  
 1004 ment, Diffusion, and Distortion of Tracers in the Ocean. *Journal of Physical  
 1005 Oceanography*, 52(12), 3221–3240. Retrieved 2022-12-02, from [https://  
 1006 journals.ametsoc.org/view/journals/phoc/52/12/JPO-D-22-0010.1.xml](https://journals.ametsoc.org/view/journals/phoc/52/12/JPO-D-22-0010.1.xml)  
 1007 (Publisher: American Meteorological Society Section: Journal of Physical  
 1008 Oceanography) doi: 10.1175/JPO-D-22-0010.1
- 1009 Döös, K., Nycander, J., & Coward, A. C. (2008). Lagrangian decomposition of the  
 1010 Deacon Cell. *Journal of Geophysical Research: Oceans*, 113(7), 1–13. (ISBN:  
 1011 0148-0227) doi: 10.1029/2007JC004351
- 1012 Döös, K., & Webb, D. J. (1994, February). The Deacon Cell and the Other Merid-  
 1013 ional Cells of the Southern Ocean. *Journal of Physical Oceanography*, 24(2),  
 1014 429–442. Retrieved 2018-05-08, from [http://journals.ametsoc.org/doi/  
 1015 abs/10.1175/1520-0485%281994%29024%3C0429%3ATDCATO%3E2.0.CO%3B2  
 1016 doi: 10.1175/1520-0485\(1994\)024\(0429:TDCATO\)2.0.CO;2](http://journals.ametsoc.org/doi/abs/10.1175/1520-0485%281994%29024%3C0429%3ATDCATO%3E2.0.CO%3B2)
- 1017 Evans, D. G., Holliday, N. P., Bacon, S., & Le Bras, I. (2023, June). Mixing and  
 1018 air–sea buoyancy fluxes set the time-mean overturning circulation in the sub-  
 1019 polar North Atlantic and Nordic Seas. *Ocean Science*, 19(3), 745–768. Re-  
 1020 trieved 2023-09-18, from [https://os.copernicus.org/articles/19/745/  
 1021 2023/](https://os.copernicus.org/articles/19/745/2023/) (Publisher: Copernicus GmbH) doi: 10.5194/os-19-745-2023
- 1022 Evans, D. G., Zika, J. D., Naveira Garabato, A. C., & Nurser, A. J. G. (2018).  
 1023 The Cold Transit of Southern Ocean Upwelling. *Geophysical Research  
 1024 Letters*, 45(24), 13,386–13,395. Retrieved 2024-02-27, from [https://  
 1025 onlinelibrary.wiley.com/doi/abs/10.1029/2018GL079986](https://onlinelibrary.wiley.com/doi/abs/10.1029/2018GL079986) (eprint:  
 1026 <https://onlinelibrary.wiley.com/doi/pdf/10.1029/2018GL079986>) doi:  
 1027 10.1029/2018GL079986
- 1028 Ferrari, R., Mashayek, A., McDougall, T. J., Nikurashin, M., & Campin, J.-  
 1029 M. (2016, July). Turning Ocean Mixing Upside Down. *Journal of  
 1030 Physical Oceanography*, 46(7), 2239–2261. Retrieved 2019-01-02, from  
 1031 <http://journals.ametsoc.org/doi/10.1175/JPO-D-15-0244.1> doi:  
 1032 10.1175/JPO-D-15-0244.1

- 1033 Ferrari, R., & Wunsch, C. (2009). Ocean Circulation Kinetic Energy: Reservoirs,  
 1034 Sources, and Sinks. *Annual Review of Fluid Mechanics*, 41(1), 253–282.  
 1035 (ISBN: 0066-4189) doi: 10.1146/annurev.fluid.40.111406.102139
- 1036 Forget, G., Campin, J.-M., Heimbach, P., Hill, C. N., Ponte, R. M., & Wun-  
 1037 sch, C. (2015, October). ECCO version 4: an integrated framework for  
 1038 non-linear inverse modeling and global ocean state estimation. *Geosci-  
 1039 entific Model Development*, 8(10), 3071–3104. Retrieved 2023-08-01, from  
 1040 <https://gmd.copernicus.org/articles/8/3071/2015/> (Publisher: Coper-  
 1041 nicus GmbH) doi: 10.5194/gmd-8-3071-2015
- 1042 Fox-Kemper, B., Adcroft, A., Böning, C. W., Chassignet, E. P., Curchitser, E., Dan-  
 1043 abasoglu, G., ... Yeager, S. G. (2019). Challenges and Prospects in Ocean Cir-  
 1044 culation Models. *Frontiers in Marine Science*, 6. Retrieved 2023-08-01, from  
 1045 <https://www.frontiersin.org/articles/10.3389/fmars.2019.00065>
- 1046 Griffies, S. M. (2024). *Geophysical Fluid Mechanics*. (Draft available at  
 1047 [https://stephengriffies.github.io/assets/pdfs/GFM\\_lectures.pdf](https://stephengriffies.github.io/assets/pdfs/GFM_lectures.pdf))
- 1048 Griffies, S. M., Adcroft, A., & Hallberg, R. W. (2020). A Primer on the Ver-  
 1049 tical Lagrangian-Remap Method in Ocean Models Based on Finite Vol-  
 1050 ume Generalized Vertical Coordinates. *Journal of Advances in Model-  
 1051 ing Earth Systems*, 12(10), e2019MS001954. Retrieved 2023-10-11, from  
 1052 <https://onlinelibrary.wiley.com/doi/abs/10.1029/2019MS001954>  
 1053 (\_eprint: <https://onlinelibrary.wiley.com/doi/pdf/10.1029/2019MS001954>)  
 1054 doi: 10.1029/2019MS001954
- 1055 Griffies, S. M., Danabasoglu, G., Durack, P. J., Adcroft, A. J., Balaji, V., Böning,  
 1056 C. W., ... Yeager, S. G. (2016, September). OMIP contribution to CMIP6:  
 1057 experimental and diagnostic protocol for the physical component of the Ocean  
 1058 Model Intercomparison Project. *Geoscientific Model Development*, 9(9), 3231–  
 1059 3296. Retrieved 2024-02-27, from [https://gmd.copernicus.org/articles/9/  
 1060 3231/2016/](https://gmd.copernicus.org/articles/9/3231/2016/) (Publisher: Copernicus GmbH) doi: 10.5194/gmd-9-3231-2016
- 1061 Griffies, S. M., Pacanowski, R. C., & Hallberg, R. W. (2000, March). Spu-  
 1062 rious Diapycnal Mixing Associated with Advection in a  $z$ -Coordinate  
 1063 Ocean Model. *Monthly Weather Review*, 128(3), 538–564. Retrieved  
 1064 2018-10-20, from [http://journals.ametsoc.org/doi/abs/10.1175/  
 1065 1520-0493%282000%29128%3C0538%3ASDMAWA%3E2.0.CO%3B2](http://journals.ametsoc.org/doi/abs/10.1175/1520-0493%282000%29128%3C0538%3ASDMAWA%3E2.0.CO%3B2) doi: 10.1175/  
 1066 1520-0493(2000)128(0538:SDMAWA)2.0.CO;2
- 1067 Groeskamp, S., Griffies, S. M., Iudicone, D., Marsh, R., Nurser, A. G., & Zika, J. D.  
 1068 (2019). The Water Mass Transformation Framework for Ocean Physics and  
 1069 Biogeochemistry. *Annual Review of Marine Science*, 11(1), 271–305. Re-  
 1070 trieved 2022-11-04, from [https://doi.org/10.1146/annurev-marine-010318-  
 1071 095421](https://doi.org/10.1146/annurev-marine-010318-095421) (\_eprint: <https://doi.org/10.1146/annurev-marine-010318-095421>)  
 1072 doi: 10.1146/annurev-marine-010318-095421
- 1073 Groeskamp, S., Zika, J. D., McDougall, T. J., Sloyan, B. M., & Laliberté, F.  
 1074 (2014, July). The Representation of Ocean Circulation and Variability in  
 1075 Thermodynamic Coordinates. *Journal of Physical Oceanography*, 44(7),  
 1076 1735–1750. Retrieved 2023-08-31, from [https://journals.ametsoc.org/  
 1077 view/journals/phoc/44/7/jpo-d-13-0213.1.xml](https://journals.ametsoc.org/view/journals/phoc/44/7/jpo-d-13-0213.1.xml) (Publisher: Ameri-  
 1078 can Meteorological Society Section: Journal of Physical Oceanography) doi:  
 1079 10.1175/JPO-D-13-0213.1
- 1080 Held, I. M., Guo, H., Adcroft, A., Dunne, J. P., Horowitz, L. W., Krasting,  
 1081 J., ... Zadeh, N. (2019). Structure and Performance of GFDL’s  
 1082 CM4.0 Climate Model. *Journal of Advances in Modeling Earth Sys-  
 1083 tems*, 11(11), 3691–3727. Retrieved 2022-12-12, from [https://  
 1084 onlinelibrary.wiley.com/doi/abs/10.1029/2019MS001829](https://onlinelibrary.wiley.com/doi/abs/10.1029/2019MS001829) (\_eprint:  
 1085 <https://onlinelibrary.wiley.com/doi/pdf/10.1029/2019MS001829>) doi:  
 1086 10.1029/2019MS001829
- 1087 Hill, C., Ferreira, D., Campin, J.-M., Marshall, J., Abernathey, R., & Barrier, N.

- 1088 (2012, January). Controlling spurious diapycnal mixing in eddy-resolving  
 1089 height-coordinate ocean models – Insights from virtual deliberate tracer  
 1090 release experiments. *Ocean Modelling*, 45-46, 14–26. Retrieved 2023-  
 1091 08-28, from [https://www.sciencedirect.com/science/article/pii/](https://www.sciencedirect.com/science/article/pii/S1463500311001880)  
 1092 S1463500311001880 doi: 10.1016/j.ocemod.2011.12.001
- 1093 Holmes, R. M., Zika, J. D., & England, M. H. (2019, January). Diathermal Heat  
 1094 Transport in a Global Ocean Model. *Journal of Physical Oceanography*, 49(1),  
 1095 141–161. Retrieved 2024-02-27, from [https://journals.ametsoc.org/view/](https://journals.ametsoc.org/view/journals/phoc/49/1/jpo-d-18-0098.1.xml)  
 1096 journals/phoc/49/1/jpo-d-18-0098.1.xml (Publisher: American Meteorolo-  
 1097 gical Society Section: Journal of Physical Oceanography) doi: 10.1175/JPO  
 1098 -D-18-0098.1
- 1099 Holmes, R. M., Zika, J. D., Griffies, S. M., Hogg, A. M., Kiss, A. E., & Eng-  
 1100 land, M. H. (2021). The Geography of Numerical Mixing in a Suite  
 1101 of Global Ocean Models. *Journal of Advances in Modeling Earth Sys-*  
 1102 *tems*, 13(7), e2020MS002333. Retrieved 2023-08-01, from [https://](https://onlinelibrary.wiley.com/doi/abs/10.1029/2020MS002333)  
 1103 onlinelibrary.wiley.com/doi/abs/10.1029/2020MS002333 (.eprint:  
 1104 <https://onlinelibrary.wiley.com/doi/pdf/10.1029/2020MS002333>) doi:  
 1105 10.1029/2020MS002333
- 1106 Hoyer, S., & Hamman, J. (2017, April). xarray: N-D labeled Arrays and  
 1107 Datasets in Python. , 5(1), 10. Retrieved 2023-08-07, from [https://](https://openresearchsoftware.metajnl.com/articles/10.5334/jors.148)  
 1108 openresearchsoftware.metajnl.com/articles/10.5334/jors.148 (Num-  
 1109 ber: 1 Publisher: Ubiquity Press) doi: 10.5334/jors.148
- 1110 Huang, R. (2005, January). Available potential energy in the world’s ocean. *Journal*  
 1111 *of Marine Research*, 63. doi: 10.1357/0022240053693770
- 1112 Ilcak, M., Adcroft, A. J., Griffies, S. M., & Hallberg, R. W. (2012, January). Spu-  
 1113 rious dianeutral mixing and the role of momentum closure. *Ocean Modelling*,  
 1114 45-46, 37–58. Retrieved 2023-08-28, from [https://www.sciencedirect.com/](https://www.sciencedirect.com/science/article/pii/S1463500311001685)  
 1115 science/article/pii/S1463500311001685 doi: 10.1016/j.ocemod.2011.10  
 1116 .003
- 1117 Iselin, C. O. (1939). The influence of vertical and lateral turbulence on the charac-  
 1118 teristics of the waters at mid-depth. *EOS*, 3, 414–417.
- 1119 Iudicone, D., Madec, G., & McDougall, T. J. (2008, July). Water-Mass Trans-  
 1120 formations in a Neutral Density Framework and the Key Role of Light Pen-  
 1121 etration. *Journal of Physical Oceanography*, 38(7), 1357–1376. Retrieved  
 1122 2023-08-28, from [https://journals.ametsoc.org/view/journals/phoc/38/](https://journals.ametsoc.org/view/journals/phoc/38/7/2007jpo3464.1.xml)  
 1123 7/2007jpo3464.1.xml (Publisher: American Meteorological Society Section:  
 1124 Journal of Physical Oceanography) doi: 10.1175/2007JPO3464.1
- 1125 Iudicone, D., Rodgers, K. B., Stendardo, I., Aumont, O., Madec, G., Bopp, L., ...  
 1126 Ribera d’Alcala’, M. (2011, May). Water masses as a unifying framework for  
 1127 understanding the Southern Ocean Carbon Cycle. *Biogeosciences*, 8(5), 1031–  
 1128 1052. Retrieved 2024-02-27, from [https://bg.copernicus.org/articles/8/](https://bg.copernicus.org/articles/8/1031/2011/)  
 1129 1031/2011/ (Publisher: Copernicus GmbH) doi: 10.5194/bg-8-1031-2011
- 1130 Jackett, D. R., & McDougall, T. J. (1997, February). A Neutral Density Vari-  
 1131 able for the World’s Oceans. *Journal of Physical Oceanography*, 27(2), 237–  
 1132 263. Retrieved 2019-01-02, from [http://journals.ametsoc.org/doi/abs/](http://journals.ametsoc.org/doi/abs/10.1175/1520-0485%281997%29027%3C0237%3AANDVFT%3E2.0.CO%3B2)  
 1133 10.1175/1520-0485%281997%29027%3C0237%3AANDVFT%3E2.0.CO%3B2 doi:  
 1134 10.1175/1520-0485(1997)027<0237:ANDVFT>2.0.CO;2
- 1135 Lee, M.-M., Coward, A. C., & Nurser, A. J. G. (2002, May). Spurious Diapyc-  
 1136 nal Mixing of the Deep Waters in an Eddy-Permitting Global Ocean Model.  
 1137 *Journal of Physical Oceanography*, 32(5), 1522–1535. Retrieved 2023-08-  
 1138 01, from [https://journals.ametsoc.org/view/journals/phoc/32/5/](https://journals.ametsoc.org/view/journals/phoc/32/5/1520-0485_2002_032_1522_sdmotd_2.0.co_2.xml)  
 1139 1520-0485\_2002\_032\_1522\_sdmotd\_2.0.co\_2.xml (Publisher: American  
 1140 Meteorological Society Section: Journal of Physical Oceanography) doi:  
 1141 10.1175/1520-0485(2002)032<1522:SDMOTD>2.0.CO;2
- 1142 Lele, R., Purkey, S. G., Nash, J. D., MacKinnon, J. A., Thurnherr, A. M., Whalen,

- 1143 C. B., ... Talley, L. D. (2021, November). Abyssal Heat Budget in the  
 1144 Southwest Pacific Basin. *Journal of Physical Oceanography*, 51(11), 3317–  
 1145 3333. Retrieved 2021-11-22, from [https://journals.ametsoc.org/view/  
 1146 journals/phoc/51/11/JPO-D-21-0045.1.xml](https://journals.ametsoc.org/view/journals/phoc/51/11/JPO-D-21-0045.1.xml) (Publisher: American  
 1147 Meteorological Society Section: Journal of Physical Oceanography) doi:  
 1148 10.1175/JPO-D-21-0045.1
- 1149 Lumpkin, R., & Speer, K. (2007). Global Ocean Meridional Overturning. *Journal*  
 1150 *of Physical Oceanography*, 37(10), 2550–2562. Retrieved from [http://dx.doi  
 1151 .org/10.1175/JPO3130.1](http://dx.doi.org/10.1175/JPO3130.1) (ISBN: 0022-3670) doi: 10.1175/JPO3130.1
- 1152 Marques, G. M., Loose, N., Yankovsky, E., Steinberg, J. M., Chang, C.-Y., Bhamidi-  
 1153 pati, N., ... Zanna, L. (2022, September). NeverWorld2: an idealized model  
 1154 hierarchy to investigate ocean mesoscale eddies across resolutions. *Geosci-*  
 1155 *entific Model Development*, 15(17), 6567–6579. Retrieved 2022-10-27, from  
 1156 <https://gmd.copernicus.org/articles/15/6567/2022/> (Publisher: Coper-  
 1157 nicus GmbH) doi: 10.5194/gmd-15-6567-2022
- 1158 Marsh, R., Nurser, A. J. G., Megann, A. P., & New, A. L. (2000, May). Water  
 1159 Mass Transformation in the Southern Ocean of a Global Isopycnal Coordi-  
 1160 nate GCM. *Journal of Physical Oceanography*, 30(5), 1013–1045. Retrieved  
 1161 2024-01-09, from [https://journals.ametsoc.org/view/journals/phoc/  
 1162 30/5/1520-0485\\_2000\\_030\\_1013\\_wmtits\\_2.0.co\\_2.xml](https://journals.ametsoc.org/view/journals/phoc/30/5/1520-0485_2000_030_1013_wmtits_2.0.co_2.xml) (Publisher: Ameri-  
 1163 can Meteorological Society Section: Journal of Physical Oceanography) doi:  
 1164 10.1175/1520-0485(2000)030<1013:WMTITS>2.0.CO;2
- 1165 Marshall, J., Jamous, D., & Nilsson, J. (1999). Reconciling thermodynamic and dy-  
 1166 namic methods of computation of water-mass transformation rates. *Deep-Sea*  
 1167 *Research Part I: Oceanographic Research Papers*, 46(4), 545–572. (ISBN: 0967-  
 1168 0637) doi: 10.1016/S0967-0637(98)00082-X
- 1169 Maze, G., Forget, G., Buckley, M., Marshall, J., & Cerovecki, I. (2009, August).  
 1170 Using Transformation and Formation Maps to Study the Role of Air–Sea Heat  
 1171 Fluxes in North Atlantic Eighteen Degree Water Formation. *Journal of Phys-*  
 1172 *ical Oceanography*, 39(8), 1818–1835. Retrieved 2023-07-21, from [https://  
 1173 journals.ametsoc.org/view/journals/phoc/39/8/2009jpo3985.1.xml](https://journals.ametsoc.org/view/journals/phoc/39/8/2009jpo3985.1.xml)  
 1174 (Publisher: American Meteorological Society Section: Journal of Physical  
 1175 Oceanography) doi: 10.1175/2009JPO3985.1
- 1176 McDougall, T., Feistel, R., Millero, F., & Jackett, D. (2009). The international  
 1177 thermodynamic equation of seawater 2010 (teos-10): Calculation and use of  
 1178 thermodynamic properties.
- 1179 McDougall, T. J., Groeskamp, S., & Griffies, S. M. (2014). On geometric aspects of  
 1180 interior ocean mixing. *Journal of Physical Oceanography*, 44, 2164–2175.
- 1181 Megann, A. (2018, January). Estimating the numerical diapycnal mixing in an  
 1182 eddy-permitting ocean model. *Ocean Modelling*, 121, 19–33. Retrieved  
 1183 2022-12-19, from [https://www.sciencedirect.com/science/article/pii/  
 1184 S1463500317301762](https://www.sciencedirect.com/science/article/pii/S1463500317301762) doi: 10.1016/j.ocemod.2017.11.001
- 1185 Molenkamp, C. R. (1968, April). Accuracy of Finite-Difference Methods Applied  
 1186 to the Advection Equation. *Journal of Applied Meteorology and Climatology*,  
 1187 7(2), 160–167. Retrieved 2023-08-25, from [https://journals.ametsoc.org/  
 1188 view/journals/apme/7/2/1520-0450\\_1968\\_007\\_0160\\_aofdma\\_2.0\\_co\\_2.xml](https://journals.ametsoc.org/view/journals/apme/7/2/1520-0450_1968_007_0160_aofdma_2.0_co_2.xml)  
 1189 (Publisher: American Meteorological Society Section: Journal of Applied  
 1190 Meteorology and Climatology) doi: 10.1175/1520-0450(1968)007<0160:  
 1191 AOFDMA>2.0.CO;2
- 1192 Nurser, A. G., & Griffies, S. M. (2019). Relating diffusive surface salinity fluxes  
 1193 to boundary freshwater and salt fluxes. *Journal of Physical Oceanography*, 49,  
 1194 2365–2376. doi: 10.1175/JPO-D-19-0037.1
- 1195 Nurser, A. J. G., Marsh, R., & Williams, R. G. (1999, July). Diagnosing  
 1196 Water Mass Formation from Air–Sea Fluxes and Surface Mixing. *Jour-*  
 1197 *nal of Physical Oceanography*, 29(7), 1468–1487. Retrieved 2023-10-

- 1198 18, from [https://journals.ametsoc.org/view/journals/phoc/29/7/](https://journals.ametsoc.org/view/journals/phoc/29/7/1520-0485_1999_029_1468_dwmffa_2.0.co_2.xml)  
 1199 1520-0485\_1999\_029\_1468\_dwmffa\_2.0.co\_2.xml (Publisher: American  
 1200 Meteorological Society Section: Journal of Physical Oceanography) doi:  
 1201 10.1175/1520-0485(1999)029<1468:DWMFFA>2.0.CO;2
- 1202 Purkey, S. G., & Johnson, G. C. (2012, September). Global Contraction of Antarctic  
 1203 Bottom Water between the 1980s and 2000s. *Journal of Climate*, *25*(17),  
 1204 5830–5844. Retrieved 2022-11-28, from [https://journals.ametsoc.org/](https://journals.ametsoc.org/view/journals/clim/25/17/jcli-d-11-00612.1.xml)  
 1205 [view/journals/clim/25/17/jcli-d-11-00612.1.xml](https://journals/clim/25/17/jcli-d-11-00612.1.xml) (Publisher: Ameri-  
 1206 can Meteorological Society Section: Journal of Climate) doi: 10.1175/  
 1207 JCLI-D-11-00612.1
- 1208 Ringler, T., Petersen, M., Higdon, R. L., Jacobsen, D., Jones, P. W., & Maltrud,  
 1209 M. (2013, September). A multi-resolution approach to global ocean model-  
 1210 ing. *Ocean Modelling*, *69*, 211–232. Retrieved 2023-12-06, from [https://](https://www.sciencedirect.com/science/article/pii/S1463500313000760)  
 1211 [www.sciencedirect.com/science/article/pii/S1463500313000760](https://www.sciencedirect.com/science/article/pii/S1463500313000760) doi:  
 1212 10.1016/j.ocemod.2013.04.010
- 1213 Saenz, J. A., Tailleux, R., Butler, E. D., Hughes, G. O., & Oliver, K. I. C. (2015,  
 1214 May). Estimating Lorenz’s Reference State in an Ocean with a Nonlinear  
 1215 Equation of State for Seawater. *Journal of Physical Oceanography*, *45*(5),  
 1216 1242–1257. Retrieved 2023-11-29, from [https://journals.ametsoc.org/](https://journals.ametsoc.org/view/journals/phoc/45/5/jpo-d-14-0105.1.xml)  
 1217 [view/journals/phoc/45/5/jpo-d-14-0105.1.xml](https://journals/phoc/45/5/jpo-d-14-0105.1.xml) (Publisher: Ameri-  
 1218 can Meteorological Society Section: Journal of Physical Oceanography) doi:  
 1219 10.1175/JPO-D-14-0105.1
- 1220 Sohail, T., Holmes, R. M., & Zika, J. D. (2023, April). Water-Mass Coordinates  
 1221 Isolate the Historical Ocean Warming Signal. *Journal of Climate*, *36*(9), 3063–  
 1222 3081. Retrieved 2023-08-01, from [https://journals.ametsoc.org/view/](https://journals.ametsoc.org/view/journals/clim/36/9/JCLI-D-22-0363.1.xml)  
 1223 [journals/clim/36/9/JCLI-D-22-0363.1.xml](https://journals/clim/36/9/JCLI-D-22-0363.1.xml) (Publisher: American Meteoro-  
 1224 logical Society Section: Journal of Climate) doi: 10.1175/JCLI-D-22-0363.1
- 1225 Stanley, G. J., McDougall, T. J., & Barker, P. M. (2021). Algorithmic Improve-  
 1226 ments to Finding Approximately Neutral Surfaces. *Journal of Advances*  
 1227 *in Modeling Earth Systems*, *13*(5), e2020MS002436. Retrieved 2023-11-30,  
 1228 from <https://onlinelibrary.wiley.com/doi/abs/10.1029/2020MS002436>  
 1229 (\_eprint: <https://onlinelibrary.wiley.com/doi/pdf/10.1029/2020MS002436>) doi:  
 1230 10.1029/2020MS002436
- 1231 Stewart, K. D., Saenz, J. A., Hogg, A. M., Hughes, G. O., & Griffiths, R. W. (2014,  
 1232 April). Effect of topographic barriers on the rates of available potential  
 1233 energy conversion of the oceans. *Ocean Modelling*, *76*, 31–42. Retrieved  
 1234 2022-12-19, from [https://www.sciencedirect.com/science/article/pii/](https://www.sciencedirect.com/science/article/pii/S1463500314000146)  
 1235 [S1463500314000146](https://www.sciencedirect.com/science/article/pii/S1463500314000146) doi: 10.1016/j.ocemod.2014.02.001
- 1236 Sverdrup, H., Johnson, M., & Fleming, R. (1942). The Oceans: Their Physics,  
 1237 Chemistry and General Biology. *Oceanography*, 1104. (arXiv: 1011.1669v3  
 1238 ISBN: 9788578110796) doi: 10.2307/210609
- 1239 Tamsitt, V., Abernathey, R. P., Mazloff, M. R., Wang, J., & Talley, L. D. (2018,  
 1240 March). Transformation of Deep Water Masses Along Lagrangian Upwelling  
 1241 Pathways in the Southern Ocean: SOUTHERN OCEAN UPWELLING  
 1242 TRANSFORMATION. *Journal of Geophysical Research: Oceans*, *123*(3),  
 1243 1994–2017. Retrieved 2019-01-02, from [http://doi.wiley.com/10.1002/](http://doi.wiley.com/10.1002/2017JC013409)  
 1244 [2017JC013409](http://doi.wiley.com/10.1002/2017JC013409) doi: 10.1002/2017JC013409
- 1245 Tesdal, J.-E., MacGilchrist, G. A., Beadling, R. L., Griffies, S. M., Krast-  
 1246 ing, J. P., & Durack, P. J. (2023). Revisiting Interior Water Mass  
 1247 Responses to Surface Forcing Changes and the Subsequent Effects on  
 1248 Overturning in the Southern Ocean. *Journal of Geophysical Research:*  
 1249 *Oceans*, *128*(3), e2022JC019105. Retrieved 2023-08-10, from [https://](https://onlinelibrary.wiley.com/doi/abs/10.1029/2022JC019105)  
 1250 [onlinelibrary.wiley.com/doi/abs/10.1029/2022JC019105](https://onlinelibrary.wiley.com/doi/abs/10.1029/2022JC019105) (\_eprint:  
 1251 <https://onlinelibrary.wiley.com/doi/pdf/10.1029/2022JC019105>) doi:  
 1252 10.1029/2022JC019105

- 1253 Toggweiler, J. R., & Samuels, B. (1998). On the Ocean’s Large-Scale Circula-  
 1254 tion near the Limit of No Vertical Mixing. *Journal of Physical Oceanog-*  
 1255 *raphy*, 28(9), 1832–1852. Retrieved from [http://dx.doi.org/10.1175/](http://dx.doi.org/10.1175/1520-0485(1998)028%3C1832:OTOSLS%3E2.0.CO%5Cn2)  
 1256 [1520-0485\(1998\)028%3C1832:OTOSLS%3E2.0.CO%5Cn2](http://dx.doi.org/10.1175/1520-0485(1998)028%3C1832:OTOSLS%3E2.0.CO%5Cn2) (ISBN: 0022-3670)  
 1257 doi: 10.1175/1520-0485(1998)028(1832:OTOSLS)2.0.CO;2
- 1258 Tziperman, E. (1986, April). On the Role of Interior Mixing and Air-Sea  
 1259 Fluxes in Determining the Stratification and Circulation of the Oceans.  
 1260 *Journal of Physical Oceanography*, 16(4), 680–693. Retrieved 2021-05-  
 1261 27, from [https://journals.ametsoc.org/view/journals/phoc/16/4/](https://journals.ametsoc.org/view/journals/phoc/16/4/1520-0485_1986_016_0680_otroim_2_0_co_2.xml)  
 1262 [1520-0485\\_1986\\_016\\_0680\\_otroim\\_2\\_0\\_co\\_2.xml](https://journals.ametsoc.org/view/journals/phoc/16/4/1520-0485_1986_016_0680_otroim_2_0_co_2.xml) (Publisher: American  
 1263 Meteorological Society Section: Journal of Physical Oceanography) doi:  
 1264 10.1175/1520-0485(1986)016(0680:OTROIM)2.0.CO;2
- 1265 Urakawa, L. S., & Hasumi, H. (2012, August). Eddy-Resolving Model Estimate  
 1266 of the Cabbeling Effect on the Water Mass Transformation in the Southern  
 1267 Ocean. *Journal of Physical Oceanography*, 42(8), 1288–1302. Retrieved 2023-  
 1268 08-25, from [https://journals.ametsoc.org/view/journals/phoc/42/8/](https://journals.ametsoc.org/view/journals/phoc/42/8/jpo-d-11-0173.1.xml)  
 1269 [jpo-d-11-0173.1.xml](https://journals.ametsoc.org/view/journals/phoc/42/8/jpo-d-11-0173.1.xml) (Publisher: American Meteorological Society Section:  
 1270 Journal of Physical Oceanography) doi: 10.1175/JPO-D-11-0173.1
- 1271 Urakawa, L. S., & Hasumi, H. (2014, February). Effect of numerical diffusion on the  
 1272 water mass transformation in eddy-resolving models. *Ocean Modelling*, 74, 22–  
 1273 35. Retrieved 2023-08-25, from [https://www.sciencedirect.com/science/](https://www.sciencedirect.com/science/article/pii/S1463500313002047)  
 1274 [article/pii/S1463500313002047](https://www.sciencedirect.com/science/article/pii/S1463500313002047) doi: 10.1016/j.ocemod.2013.11.003
- 1275 Walin, G. (1982, January). On the relation between sea-surface heat flow and ther-  
 1276 mal circulation in the ocean. *Tellus*, 34(2), 187–195. Retrieved 2020-02-10,  
 1277 from <https://doi.org/10.3402/tellusa.v34i2.10801> doi: 10.3402/tellusa.  
 1278 v34i2.10801
- 1279 Winters, K. B., Lombard, P. N., Riley, J. J., & D’Asaro, E. A. (1995, April).  
 1280 Available potential energy and mixing in density-stratified fluids. *Journal*  
 1281 *of Fluid Mechanics*, 289, 115–128. Retrieved 2021-06-09, from [https://www](https://www.cambridge.org/core/journals/journal-of-fluid-mechanics/article/available-potential-energy-and-mixing-in-densitystratified-fluids/A45F1A40521FF0A0DC82BC705AD398DA)  
 1282 [.cambridge.org/core/journals/journal-of-fluid-mechanics/article/](https://www.cambridge.org/core/journals/journal-of-fluid-mechanics/article/available-potential-energy-and-mixing-in-densitystratified-fluids/A45F1A40521FF0A0DC82BC705AD398DA)  
 1283 [available-potential-energy-and-mixing-in-densitystratified-fluids/](https://www.cambridge.org/core/journals/journal-of-fluid-mechanics/article/available-potential-energy-and-mixing-in-densitystratified-fluids/A45F1A40521FF0A0DC82BC705AD398DA)  
 1284 [A45F1A40521FF0A0DC82BC705AD398DA](https://www.cambridge.org/core/journals/journal-of-fluid-mechanics/article/available-potential-energy-and-mixing-in-densitystratified-fluids/A45F1A40521FF0A0DC82BC705AD398DA) (Publisher: Cambridge University  
 1285 Press) doi: 10.1017/S002211209500125X
- 1286 Zika, J. D., England, M. H., & Sijp, W. P. (2012, May). The Ocean Circulation  
 1287 in Thermohaline Coordinates. *Journal of Physical Oceanography*, 42(5),  
 1288 708–724. Retrieved 2023-08-31, from [https://journals.ametsoc.org/](https://journals.ametsoc.org/view/journals/phoc/42/5/jpo-d-11-0139.1.xml)  
 1289 [view/journals/phoc/42/5/jpo-d-11-0139.1.xml](https://journals.ametsoc.org/view/journals/phoc/42/5/jpo-d-11-0139.1.xml) (Publisher: Ameri-  
 1290 can Meteorological Society Section: Journal of Physical Oceanography) doi:  
 1291 10.1175/JPO-D-11-0139.1
- 1292 Zika, J. D., & Taimoor, S. (2023, July). An optimal transformation method  
 1293 for inferring ocean tracer sources and sinks. *EGUsphere*, 1–25. Re-  
 1294 trieved 2024-02-27, from [https://egusphere.copernicus.org/preprints/](https://egusphere.copernicus.org/preprints/2023/egusphere-2023-1220/)  
 1295 [2023/egusphere-2023-1220/](https://egusphere.copernicus.org/preprints/2023/egusphere-2023-1220/) (Publisher: Copernicus GmbH) doi:  
 1296 10.5194/egusphere-2023-1220